JMEPEG (2022) 31:2391–2409
https://doi.org/10.1007/s11665-021-06329-4


1059-9495/$19.00

# Characterization of Friction Stir-Welded Polylactic Acid/Aluminum Composite Primed through Fused Filament Fabrication

*Ranvijay Kumar, Nishant Ranjan, Vinay Kumar, Raman Kumar, Jasgurpreet Singh Chohan, Aniket Yadav, Piyush, Shubham Sharma, Chander Prakash, Sunpreet Singh, and Changhe Li*

Submitted: 16 May 2021 / Revised: 11 September 2021 / Accepted: 25 September 2021 / Published online: 18 October 2021

**There are many possible reasons for low weld strength in FSW of thermoplastic; low thermal conductivity, high energy losses in friction stir welding (FSW), material spill-out, involvement of high mechanical forces, etc. To counter strike the above-mentioned issues which weaken the joint's strengths, two strategies have been approached. The first approach is based upon the preparation of aluminum (Al) layers-reinforced Polylactic acid (PLA)/Al composite material which must have high thermal conductivity and crystallinity for improved heat generation in FSW. In the second approach, the FSW has been performed using a semi-consumable pin of similar materials which can compensate for the materials loss and void formation during FSW. Alternating layer composite of (PLA)/Al was manufactured by modified fused filament fabrication (FFF) 3D printing process then welded by FSW process in next steps. In this study, the FSW process was performed by using a semi-consumable pin profile of PLA with varying tool rotation speed (TRS) (800, 1100, and 1400rpm), depth of semi-consumable pin (SPD) (2, 3 and 4 mm), and transverse speed (TVS) (20, 30 and 40mm/min). FSW joints were subjected to mechanical (tensile strength, percentage elongation, and modulus of toughness), morphological (fracture by scanning electron microscopy and surface profiling), structural (Fourier-transform infrared spectroscopy, x-ray diffraction) for optimizing the FSW process parameters. Analytic hierarchy process and genetic algorithm are implemented to acquire a single set of parameters which would result in the best value of tensile properties. The suggested levels are 1400 rpm, 2 mm, and 31.79 mm/min. of TRS, SPD, and TVS, respectively.**

**Keywords** FSW, hybrid composites, morphology, PLA, welding defect

## 1. Introduction

The conventional FSW is a process of joining two similar or dissimilar materials using a non-consumable process. The process is best known for the joining of parts under the melting point of the materials, low cost of joining and as a low-energy intensive process. The parameters such as rotational speed of pin, pin depth, pin diameters, stirring time, transverse speed, pin angle and materials of pin profile are the important

**Ranvijay Kumar, Nishant Ranjan, Raman Kumar, Jasgurpreet Singh Chohan, Aniket Yadav,** and **Piyush**, Department of Mechanical Engineering, Chandigarh University, Chandigarh, Punjab, India; **Vinay Kumar**, Department of Production Engineering, Guru Nanak Dev Engineering College, Ludhiana, India; **Shubham Sharma**, Department of Mechanical Engineering, IK Gujral Punjab Technical University, Jalandhar-Kapurthala Road, Kapurthala 144603 Punjab, India; **Chander Prakash**, School of Mechanical Engineering, Lovely Professional University, Phagwara, Punjab, India; **Sunpreet Singh**, Department of Mechanical Engineering, Chandigarh University, Chandigarh, Punjab, India; and Department of Mechanical Engineering, National University of Singapore, Singapore, Singapore; and **Changhe Li**, School of Mechanical and Automotive Engineering, Qingdao University of Technology, Qingdao 266520, China. Contact e-mail: snprt.singh@gmail.com.

**Abbreviations**

| | |
|---|---|
| ABS | Acrylonitrile butadiene styrene |
| AHP | Analytic hierarchy process |
| Al | Aluminum |
| AM | Additive manufacturing |
| EDS | Energy-dispersive x-ray spectroscopy |
| FFF | Fused filament fabrication |
| FSW | Friction-stir welding |
| FTIR | Fourier-transform infrared spectroscopy |
| FTS | Fracture tensile strength |
| FWHM | Full width half maxima |
| GA | Genetic algorithm |
| MOT | Modulus of toughness |
| PC | Polycarbonate |
| PEB | Percentage elongation at break |
| PEEK | Poly-ether-ether ketone |
| PMMA | Poly(methyl methacrylate) |
| PLA | Polylactic acid |
| PPS | Polyphenyl sulfone |
| SEM | Scanning electron microscopy |
| SPD | Semi-consumable pin depth |
| STL | Standard Tessellation Language |
| TPU | Thermoplastic Polyurethane |
| TRS | Tool rotational speed |
| TVS | Transverse speed |
| UTM | Universal testing machine |
| UTS | Ultimate tensile strength |
| XRD | X-ray diffraction |

considerations for the FSW process. In recent times, friction welding of thermoplastics has been one of the most investigated disciplines in polymer works. Lambiase et al. (2020) made broad assessment of latter advancements on mechanical behavior, process parameters, quality assessment and further scope of expansion in domain in future (Ref 1). Derazkola et al. (2018) have investigated the influence of pin profiles in FSW. Three different pin profiles (frustum, triangle and cone) were used. The best results were observed in frustum-shaped pin profiles, profile pins having larger surface area formed defect-free weld and edged type profile represented tunnel defect (Ref 2). Previous investigators have used sheet lamination method of friction welding for Poly(methyl methacrylate) (PMMA) matrix reinforced with steel layers. This reinforcement of steel in PMMA resulted in superior flexural bending, depicted using ultimate tensile test (Ref 3). It has been studied theoretically and experimentally the effect of processing parameters like angle of tool tilt, depth of plunge, tool rotation speed (w) and transverse velocity. A combination of low tool plunge depth with low tilt angle offers optimum material flow to form defect-free joints. By using high tool rotational speed with low linear velocity, the formation of defects may be minimized (Ref 4). It has been performed experiments to check the influence of tool rotation (1000, 1250 and 1600 mm) and transverse speed (25 and 50 mm/min) in FSW of PMMA. The highest flexural and tensile strength were obtained at transverse speed of 25 mm/min and 1600 rpm of tool rotation (Ref 5). Previous investigator has developed a relation between process parameters and polycarbonate sheet material properties after performing FSW. Effect of plunge depth, traveling speed, tilt angle and tool rotational speed were investigated. Major observations revealed in experiment show that at very high and low heat inputs defect-free welds cannot be prepared (Ref 6). It has been investigated thermomechanical models using simulation method. The effect of rotational speed was investigated on polycarbonate material. It was found that increasing rotational speed reduces the temperature gradient, resulting in less probability of crack formation near joint (Ref 7). The study has been conducted for thermomechanical simulation of FSW-welded PMMA. Effects of tilt angle and plunge depth were analyzed, and simulation results disclosed that higher tilt angle and plunge depth bring about high frictional heat (Ref 8). The previous investigators have used 3D thermochemical mechanical numeric model to simulate underwater FSW of a polymer. Experiments were performed on polycarbonate material to validate the findings of simulation method. It was found that crystallinity and chemical changes in submerged state were lower than the conventional friction weld joint (Ref 9). It has been used novel powder fed friction stir process, which facilitates the creation of polymer matrix nanocomposites. Polycarbonate-based nanocomposites with alumina nanocomposites were reinforced and which depicted higher tensile strength but lesser flexural strength than the polycarbonate matrix (Ref 10). The previous study has been conducted for preparation of PMMA reinforced with alumina (20 %vol) using friction stir welding. Defect-free nanocomposite at optimum settings ( rotational speed of 1600 rpm and transverse speed of 120 mm/m) was formed. 10%-20% increases in toughness and strength were observed in comparison with the non-treated PMMA (Ref 11).

Researchers have extensively used PLA for the development of composites for various applications by FFF-based 3D printing. It has been noticed that mechanical, thermal, and electrical properties are enhanced with the addition of reinforcements with suitable concentrations. FFF has brought a paradigm shift in rapid tooling, which is further strengthened by the inclusion of composite materials available for extrusion (Ref 12, 13). The manufacturing of small/limited size parts is one of the major issues related to FFF processes. In most of the commercially available FFF-based 3D printers, there is a limitation for size which restricts the application domain of the process, to overcome this issue, FSW of such FFF parts is one of the foolproof techniques. The implication of FSW for FFF parts extends the application domain for various sectors. Recently, researchers have tried to join the FFF parts through FSW for various structural, automotive, and aerospace applications. The studies have been performed on welding of acrylonitrile butadiene styrene (ABS), PLA, and polyether ether ketone (PEEK) materials extensively (Ref 14, 15). As per the necessities concern, friction-assisted welding for thermoplastic-based materials has been explored in the recent past with maintaining mechanical strength and minimizing defects in welded products. The unwanted chip formation and uncontrolled materials flow are issues that occur due to low heat formation in the FSW of thermoplastic materials due to low thermal conductivity itself. To overcome these issues Nath et al. (2021) and Singh et al. (2020) have suggested the use of the novel self-heated FSW tool when joining (Ref 16, 17). The joining of two dissimilar thermoplastics is quite tough due to the mismatch in their glass transition, melting point, crystallinity, thermal conductivity, and various rheological properties. It has been explored a way to frictionally weld the two dissimilar types of thermoplastics (e.g., ABS and polyamide 6 (PA6)) by maintaining the similar melt flow index (MFI) in the repair of leakages/cracks in oil/gas pipelines (Ref 18). Using the consumable tool of the MFI compatible thermoplastic is one of the alternative ways to join thermoplastics with maintaining good mechanical properties and very few defects (Ref 19, 20). Lambiase et al. (2020) have been reported varying the tilt angle in FSW of polycarbonate (PC) sheets helps in controlling the defects (Ref 21). Sharma et al. (2020) have been studying the effects of the tool speed, transverse speed, and pin profile (cylindrical, threaded, and conical) on the tensile strength of the PLA welds manufactured by the FSW process (Ref 22). Since PLA is one of the most economical and easily available thermoplastics materials with good mechanical properties, it has been used in various scaffolding applications. FSW of 3D printed PLA structure may be used in biomedical applications for repair/surgery prospective. The mechanical properties of friction-welded metal matrix composites, powder metals, titanium alloys, and copper alloys are extensively studied in the last three years. However, it can be deduced that minimal work has been done using Al particles and especially hybrid metal sprayed/FFF process. In recent years FFF-based techniques have been employed for the 3D printing of PLA-based thermoplastics composites for applications in medical, engineering, and biomedical applications (Ref 23-26). The evolution of such techniques can be very helpful for repairing scaffolds by FSW practice.

Literature is evident that PLA-based thermoplastic composites material has a great range of functionalities for its applications in automobile, aerospace, construction, biomedical, tissue engineering, packaging, robotics, electrical and sensors, and frequency shielding applications. AM technologies have emerged as established tools for processing PLA-based composites in such applications. FSW of those AM components

is highly appreciated for such application. Previous studies have reported FSW of AM thermoplastic composites with the investigation of mechanical, thermal, and morphological properties. But to maintain the sustainable mechanical properties of FSW, welded AM components have been less reported. The Al film deposition method has been applied in between the PLA matrix for modifying the tensile properties and to support better heat generation/materials flow in this study.

## 2. Materials and Method

In this study, hybrid PLA/Al composite structures were prepared using 1.75mm PLA feedstock filaments (Make: Shenzhen Sunhokey Electronics Co., Ltd, Shenzhen, China). The properties of PLA are given in Table 1. The density of natural PLA polymers is 1.210-1.430 g/cm$^3$, and tensile strength varies between 61 and 66 MPa. The glass transition temperature is 50-80 °C and melting temperature varies between 130 °C and 180 °C. The method for manufacturing hybrid structures has been adopted from studies conducted by Kumar et al. (2020) (Ref 27, 28). The Al metal spray deposited in between the additive layers was procured in the form of compressed liquid (Make: Wurth India Ltd, India). Al metal spray was specified with 50$\mu$m dry layer thickness and density of 1.15 g/cm$^3$. Al metal spray consists of 99.9% commercially pure Al particles mixed in acrylated alkyd resin and is recommended to use up to 250°C temperatures (Ref 29).

The SEM and energy-dispersive x-ray spectroscopy (EDS) analysis of Al metal spray has been performed to check the size, shape and composition of the Al spray selected as the reinforcement material (Please see Fig. 1a and b). The data reveal that size of the Al spray ranged between 2.068 and 7.121 $\mu$m with irregular round shape formation. The Al spray consists of 75.51% (mass%) Al and 24.49% (mass%) of Oxygen.

For this research study, firstly hybrid composites structures of PLA and Al have been prepared using a modified FFF process in the rectangular substrate and cylindrical semi-consumable pin profiles that are shown in Fig. 2(a) and (b). In Fig. 2(c) it has been shown that a semi-consumable pin profile was fixed in the shoulder of the FSW setup. Figure 2(d) shows the welded PLA and Al hybrid structure by the FSW process. Further, the welded structures were processed and cut into the required dimension for mechanical (tensile properties), morphological (SEM and optical microscopy), and structural (XRD and FTIR) properties investigations.

**Table 1 Physical and thermal properties of PLA**

| Properties | Value | Refs. |
|---|---|---|
| Density | 1.210-1.430 g/cm$^3$ | 30 |
| Tensile strength | 61 MPa-66 MPa | 31 |
| Glass transition temperature | 50-80 °C | 32 |
| Melting temperature | 130-180 °C | 33 |
| Recommended printing temperature | 180-230 °C | 34 |
| Recommended printing speed | 30 mm-90 mm/sec | 35 |
| Viscosity | 0.265-0.467 M Ps-s | 36 |

## 3. Experimentation

### 3.1 Composite Development

Figure 3 depicts schematics of the hybrid FFF process to form PLA/Al layers of composites structures. A commercial FFF-based 3D printer (Make: Pruss i3: Model: MK2, maximum nozzle temperature: 400) was used to manufacture the PLA/Al composite structure. The processing method for composite formation has been adopted from the previous studies conducted by Kumar et al. (2020) (Ref 27, 28). Al metal spray supplier claimed 50$\mu$m layer thickness of Al metal spray deposits in one complete back and forth motion (Ref 29). Kumar et al. (2020) have been suggested that the mechanical properties of PLA/Al composite structure are maximized if it processes by keeping 100% infill density and 60 °C, barrel temperature, 0.1 mm layer thickness, 3 number of outer perimeters, 45°Infill angle, rectilinear fill pattern, 0.4 mm nozzle diameter with 5 number of in-between spray layers (Ref 28). Also, a stand-off distance of 150 mm has been maintained between the substrate and spay cylinder during the spraying process. The static stand-off distance has been maintained during the spraying process to ensure the uniform deposition of the Al on the PLA surface. On the suggested FFF parameters, PLA/Al substrates have been prepared in 60mm×30mm×4mm dimension sheets. The cylindrical semi-consumable pin profile (diameter: 3mm and length: 50mm) was also prepared using similar FFF process parameters.

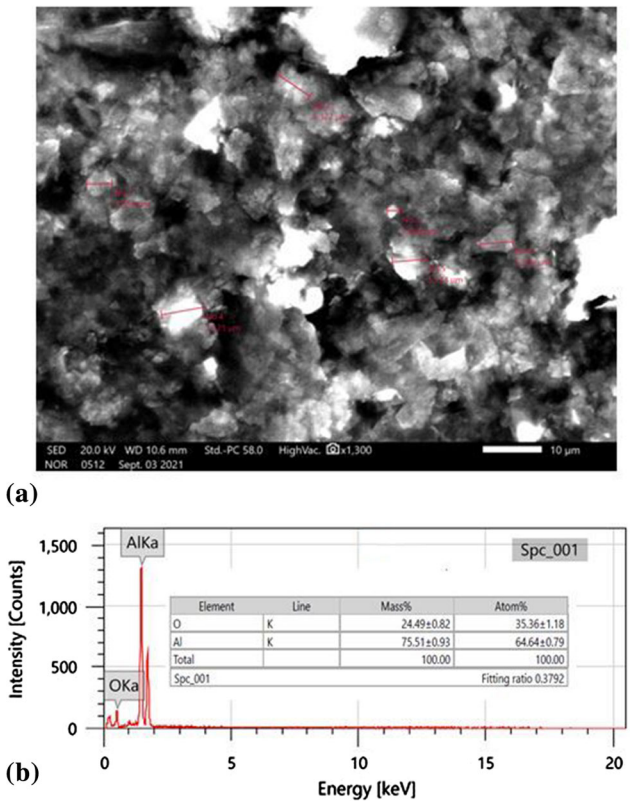


**Fig. 1** (a) SEM micrograph of al spray and (b) EDS plot of Al spray

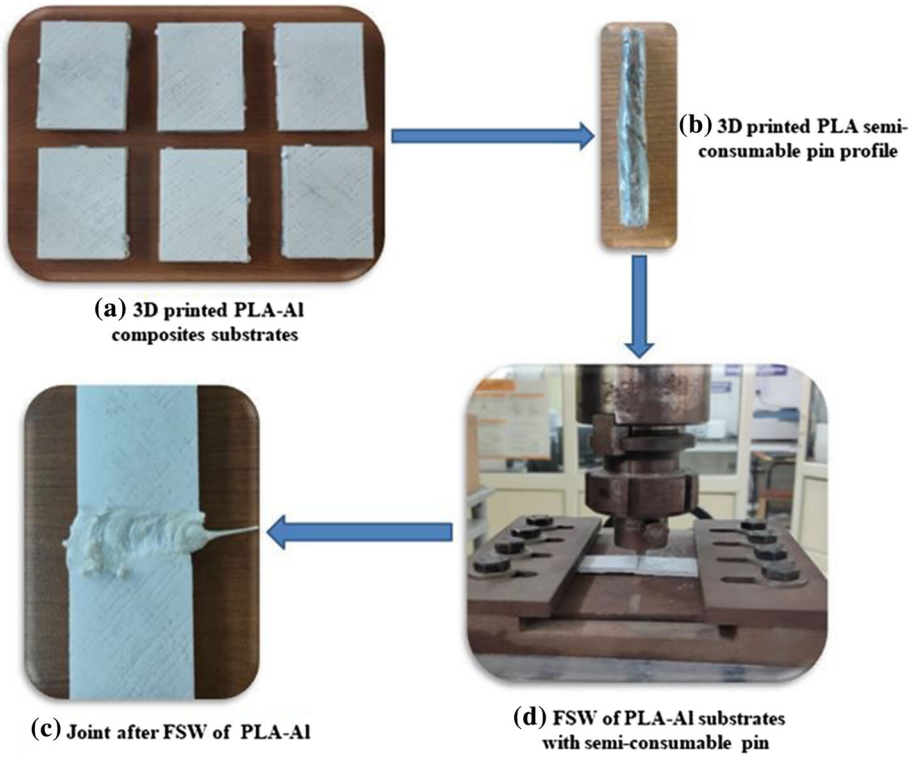


**Fig. 2** Process methodology for FSW of PLA and Al composite structures (a) 3D printed substrate, (b) 3D printed semi-consumable pin profile, (c) Working procedure of FSW, (d) FSW manufactured joint

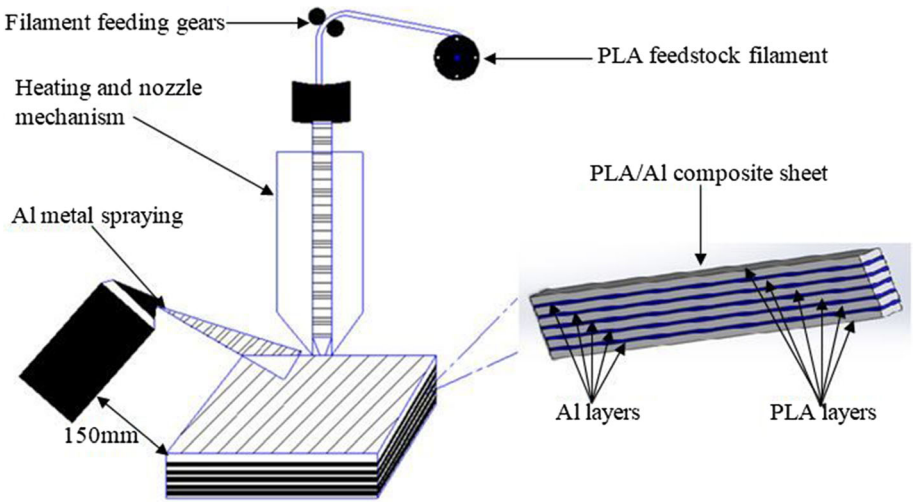


**Fig. 3** Schematic for manufacturing of PLA/Al composite structures

### 3.2 FSW of PLA/Al Composites

A vertical milling setup (Customized with maximum TRS: 2000 rpm; maximum TVS: 100mm/min)) configured with electronic tool rotation speed control has been used for FSW of PLA/Al substrates. The tool's shoulder-pin arrangement has been modified in a way so that it can increase or decrease the length of the pin profile exposed interface of substrates. The shoulder has been configured with a facility to lock and unlock the pin profile from both directions (from up and side). Inserted pin profile was tightened by a screw lock from both sides of the shoulder. In this study, the shoulder diameter was fixed to 20mm, and a cylinder PLA pin of 3 mm was fixed to it (see Fig. 4).

In the FSW, there is a significant material loss occurs during the process due to shoulder movement, which pushes materials to flow outside to the interface. The aim of facilitating the semi-consumable to regulate the materials flow at the interface during the FSW process to restrict the void and crack formation since materials usually spill out to the outer side of the

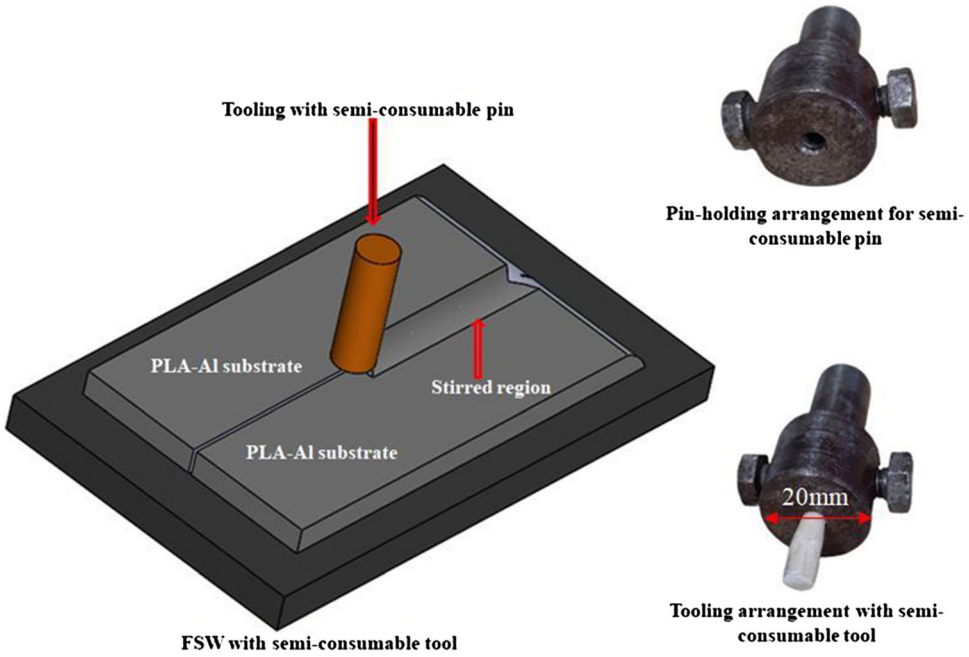


**Fig. 4** Schematic for FSW of PLA/Al composite substrate using semi-consumable PLA tool

**Table 2 Experimental design for FSW of PLA/Al composites**

| Sample No. | TRS | SPD | TVS |
|---|---|---|---|
| 1 | 800 rpm | 2 mm | 20 mm/min |
| 2 | 800 rpm | 3 mm | 30 mm/min |
| 3 | 800 rpm | 4 mm | 40 mm/min |
| 4 | 1100 rpm | 2 mm | 30 mm/min |
| 5 | 1100 rpm | 3 mm | 40 mm/min |
| 6 | 1100 rpm | 4 mm | 20 mm/min |
| 7 | 1400 rpm | 2 mm | 40 mm/min |
| 8 | 1400 rpm | 3 mm | 20 mm/min |
| 9 | 1400 rpm | 4 mm | 30 mm/min |

interface. This modified shoulder-pin setup regulates the flow of PLA to the interface of PLA/Al substrate to minimize the defects caused by materials spill-out.

FSW for joining 3D printed PLA/Al substrates was performed as per the design of the experiment given in Table 2. FSW parameters such as TRS (800, 1100, and 1400 rpm), SPD (2, 3, and 4 mm), and TVS (20, 30, and 40 mm/min) have been controlled to execute joining. The range of TRS was selected based upon the fact that below 800 rpm it was unable to get a well-mixed stirred region (defected weld joint), and above 1400 rpm, it degraded the substrate due to high heat generation (defected weld joint). The maximum SPD was selected upon the thickness of the PLA/Al substrate (4 mm). The PLA pin was filled to half (2mm), three fourth (3 mm), and full profile (4 mm) of the PLA/Al substrates. The level of TVS was selected based upon the pilot experimentation. Below 20 mm/min TVS, welded pieces were observed with some degradation, whereas above 40 mm/min, it has appeared with non-mixed joint interfaces.

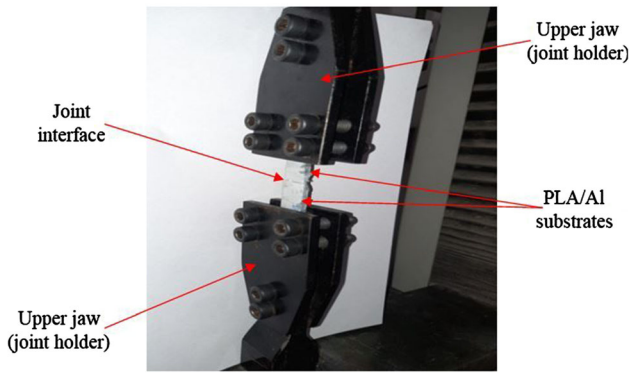


**Fig. 5** FSW-welded joint claimed to jaws of UTM

### 3.3 Mechanical Characterization

**3.3.1 Tensile Testing.** First, FSW-welded joints were cut into the required shape for tensile testing. Then, a universal testing machine (make: Shanta Engineering) of 5000N maximum load capacity has been taken to fracture the FSW-welded samples. A strain rate of 50 mm/min with grip separation of 52 mm was maintained for tensile fracture of FSW samples. Tensile testing was conducted to obtain the results in the form of the ultimate tensile strength (UTS), fracture tensile strength (FTS), percentage elongation at break (PEB), and modulus of toughness (MOT). Figure 5 shows the fixture of tensile testing on which upper and lower jaws hold the sample. It should be noted that each joint has been tested three times to minimize the experimental errors.

### 3.4 Morphological Characterization

The morphological characterization has been performed to investigate the fracture mechanism by SEM, structural and compound identification by XRD, and FTIR.

**3.4.1 SEM.** FSW-welded PLA/Al composites joints that underwent tensile fractures were analyzed by SEM. Micrographic observations have been taken to investigate the effect of conducting FSW process parameters on joint strength. SEM setup (Make: Jeol, Japan; Model: JSM: IT 500) has been used to take the photomicrographs of fracture joints at ×25 and ×50 magnifications. The observations were taken under vacuum mode while providing a power supply of 15V. It should be noted that an EDS extension of SEM was used for the identification of elements at the fracture region.

**3.4.2 XRD.** XRD is a rapid analysis method that can provide information on unit cell dimensions and is mainly used for the phase identification of crystalline materials. Constructive interference of monochromatic x-rays and a crystalline sample is the basis of XRD. A cathode-ray tube produces the x-rays, which are then filtered to produce monochromatic radiation, collimated to focus the beam, and guided at the sample. When Bragg's Law ($n\lambda=2d\sin\theta$) is satisfied, positive interference (and a diffracted ray) results from the interaction of incident rays with the sample. The wavelength of electromagnetic radiation is related to the diffraction angle and lattice spacing in a crystalline sample by this law. The observed, processed, and counted diffracted x-rays are then analyzed. Due to the random orientation of the solid and powdered material, scanning the sample across a range of 2θ angles should yield all possible lattice diffraction directions. Since each material (metal, polymer, or any minerals) has its own set of d-spacings, converting the diffraction peaks to d-spacings allows mineral identification. This is usually accomplished by comparing d-spacings to regular reference patterns. The generation of x-rays in an x-ray tube is the basis for all diffraction methods. The diffracted rays are obtained after the x-rays are focused on the sample. The angle between the incident and diffracted rays is a critical component of all diffraction. Beyond that, the instrumentation for powder and single-crystal diffraction differs.

In this study, D8 ADVANCE ECO (manufactured by—BRUKER; Billerica, Massachusetts, United States) has been used to analyze all three samples (Neat PLA, best tensile strength joint, and least tensile strength joint). In this research work, 2θ angles vs. intensity graph have been plotted with a wavelength value of 1.54060Å. As the sample and detector were rotated, the intensity of the reflected x-rays was recorded. Data have been collected at 2θ range from ∼10° to 100.397° angles. By using the XRD method, %age crystallinity and %age amorphous have been calculated. XRD measured the crystal structure of all three joints samples with Cu-Kα radiation (wavelength (λ) = 1.54060Å) at 40 kV and 25 mA.

**3.4.3 FTIR.** IR spectroscopy based upon Fourier transformation was performed for neat FSW PLA sample, best and worst FSW PLA composite samples using Analytical INFRA 3000B FTIR spectrometer. The infrared rays fall over the cross-sectional surface of FSW PLA, sample 2 and sample 7 obtained after performing UTM testing. Figure 6 shows the schematics of FTIR testing of FSW specimens. The changes produced in bonding characteristics of PLA before and after coating were obtained.

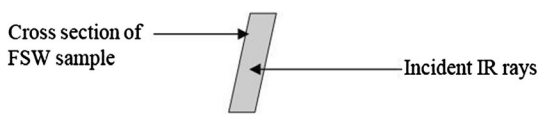


**Fig. 6** Schematics for FTIR of FSW PLA samples

**3.4.4 Surface Rendering.** The photo-micrographic observations were taken through SEM and were further processed through a surface rendering software package (Gwyddion, version: 2.56). This analysis has been done to investigate the fracture surface morphology and ideas about failure fashion (ductile vs. brittle fracture). The rendering of photomicrographs has been performed using the smoothening filter of full-width half maxima (FWHM). The FWHM has been calculated by using a standard deviation (σ) in the fracture surface. The mean of a mean of distribution has been assumed 0 for the rendering of the surface. See the given expression (Eq 1)

$$\mathrm{FWHM} = 2\sqrt{(2\ln 2)}\sigma = 2.3548\sigma \quad \text{(Eq 1)}$$

## 4. Results and Discussion

### 4.1 Tensile Properties

The tensile loading on PLA-/Al-welded parts has resulted in a complete fracture from the interface of joints. The observations have been taken in the form of UTS, FTS, PEB, and MOT (see Table 3). It has been observed to have maximum UTS (34.63 MPa) and FTS (31.17 MPa) for sample 7, whereas minimum UTS (5.72 MPa) and FTS (5.15 MPa) for sample 2. The tensile strength in the case of sample 7 was exhibited due to the combination of higher TRS (1400 rpm) and TVS (40 mm/min), which provided better heat generation at the joint interface to promote the stirring/fusion. On the other hand, insufficient heat formation due to lower TRS (800 rpm) and TVS (30 mm/min) was unable to produce adequate heat for stirring, so that it has been observed as minimum tensile strength for sample 2. The maximum strength has been observed for sample 7, so that neat PLA materials have also been welded on the same parametric setting. UTS (22.15 MPa) and FTS (19.83 MPa) of neat PLA were observed less than PLA/Al joints of sample 7. Higher UTS and FTS in the case of PLA/Al sample compared to the neat PLA sample due to the addition of in-between Al layers. The addition of Al layers may have contributed to the higher heat formation (due to higher thermal conductivity of Al) during the FSW process, which encouraged the better fusion of the joints. There may be more possible reasons for getting higher strength for sample 7 as compared to the neat PLA sample and other samples. The low thermal conductivity of neat PLA is one of the reasons that is why lower tensile properties have been observed. Moreover, the Al reinforcement in the case of PLA/Al composition of sample 7 has increased the crystallinity so that it has attained the maximum tensile strength. Despite this fact, the right process parametric combination in the case of sample 7 has also increased the uniformity/dispersion of Al which leads to better heat generation resulting in higher tensile strength. The involvement of proper heat generation at the interface of the joints has smoothened the materials flow which provided the adequate mechanism for control of materials flow in case of the sample which has higher tensile strength. On the other hand,

**Table 3 Tensile properties of PLA/Al joints**

| Sample | UTS, MPa | FTS, MPa | PEB, % | MOT= (1/2× UTS × strain at PEB), MPa |
|---|---|---|---|---|
| 1 | 23.47 ± 0.24 | 21.12 ± 0.25 | 5 ± 0.0 | 0.608 |
| 2 | 5.72 ± 0.04 | 5.15 ± 0.05 | 1 ± 0.0 | 0.019 |
| 3 | 14.94 ± 0.12 | 13.44 ± 0.11 | 2 ± 0.0 | 0.154 |
| 4 | 30.57 ± 0.42 | 27.51 ± 0.40 | 4 ± 0.0 | 0.686 |
| 5 | 5.92 ± 0.08 | 5.33 ± 0.09 | 1 ± 0.0 | 0.030 |
| 6 | 11.9 ± 0.21 | 10.71 ± 0.22 | 3 ± 0.0 | 0.184 |
| 7 | 34.63 ± 0.78 | 31.17 ± 0.76 | 4 ± 0.0 | 0.657 |
| 8 | 6.71 ± 0.18 | 6.04 ± 0.16 | 1 ± 0.0 | 0.034 |
| 9 | 13.53± 0.20 | 12.18 ± 0.21 | 2 ±0.0 | 0.163 |
| Neat PLA joint | 22.15± 0.24 | 19.93 ± 0.25 | 4± 0.0 | 0.460 |

Results of tensile properties are the average of three repeated experiments

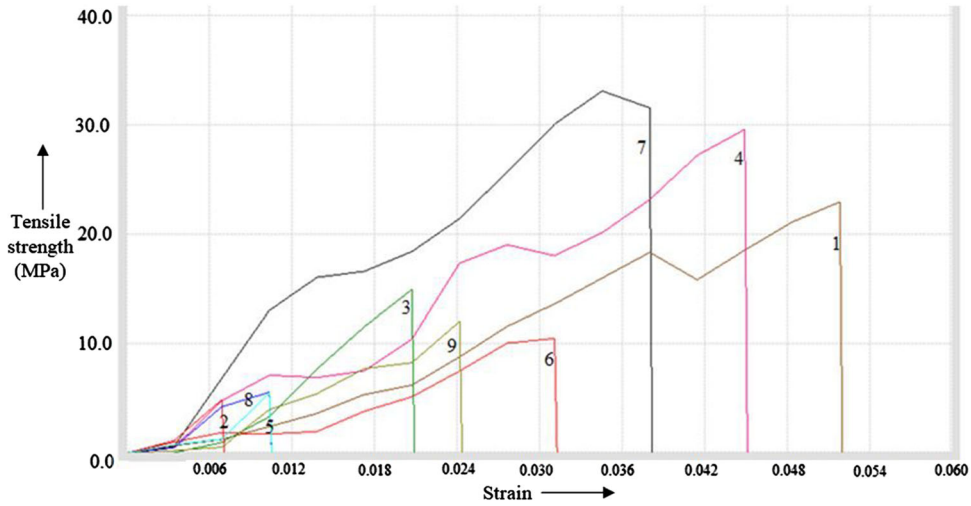


**Fig. 7** Stress vs. strain curves of fractured PLA/Al joints

the strength of sample 2 has been observed due to that low rotational speed is unable to produce adequate heat to regulate the materials flow which leads to weakening the tensile strength.

Figure 7 shows the stress vs. strain curves for fractured PLA/Al joints. The MOT is the measure of how much joints can sustain if crash loading is applied. The better resistance against crashes makes welded joints more acceptable for structural/construction applications. It should be noted that MOT is dependent on the value of both UTS and PEB. As the value of UTS and PEB is given in Table 3, the MOT of the joints has been calculated. It has been observed to have maximum MOT in sample 7 (0.657 MPa) and minimum in sample 2 (0.019 MPa). The results show that sample 7 has maximum resistivity against crash loading.

### *4.2 Surface and Fracture Morphology of Welded Pieces*

**4.2.1 Optical Photomicrographs of a Stirred Surface Region.** Figure 8 shows the optical photomicrographs of stirred surfaces of PLA/Al joints manufactured by the FSW process. A non-uniformly mixed surface with broken/cracked layers has been noticed in the case of sample 2 to identify the cause for minimum UTS and FTS. Also, the surface of welded sample 2 can be considered defective due to a lack of heat generation at the interface (primarily due to low TRS of tool: 800rpm). The stirred surface in the case of welded sample 7 has been noticed with well-established structures of uniform mixing with minimum surface defect (low porosity and cracks), which confirms the causes for getting maximum UTS and FTS in the case of welded sample 7. The well and uniform surface/interface mixing were possible due to the high TRS of pin profile (1400 rpm) in the case of sample 7, which provided adequate heat generation for well stirring. Similarly, UTS and FTS of sample 5, sample 6, and sample 8 have been noticed similar to sample 2. It can be observed from the photomicrographs of sample 5, sample 6, and sample 8 that the mixing of surfaces was not proper due to variation of input process parameters. These parametric combinations have led to the generation of porosity and cracks (due to improper mixing) on the surface, which minimized the UTS and FTS values. On the other hand, uniform mixing has been noticed in sample 1, sample 3, sample 4, and sample 9, with the low significance of cracks and porous holes, confirming higher UTS and FTS. The formation of void and cracks mainly occur due to improper materials flow during the stirring process in FSW. Materials flow is controlled by the action of heat generation due to parametric combination, the thermal conductivity of the materials, and temperature-dependent rheology. In this case,

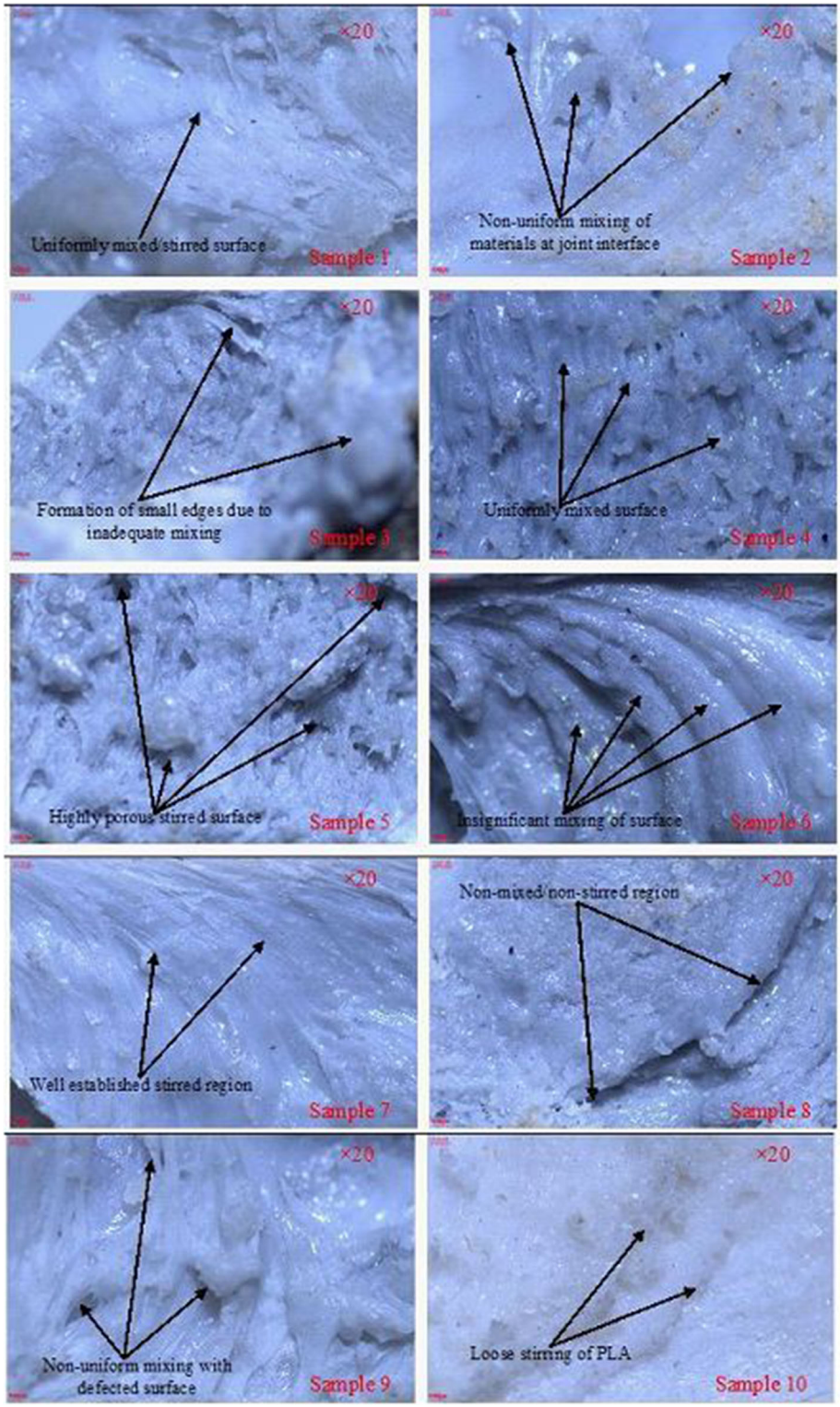


**Fig. 8** Optical photomicrographs of stirred surfaces of PLA/Al joints (×20 magnification)

inadequate heat generation caused by low TRS (800rpm) has maximized the formation of the voids in the case of joint sample 2. In the case of the neat PLA sample, low thermal conductivity and low crystallinity were responsible. Voids and cracks are visible in micrographs of joint sample 2 and neat PLA joints (see Fig. 8). On the different aspects, adequate heat was generated in the case of joint sample 7 which maximized the tensile strength. This prediction for varying tensile strength of joints may be predicted from the flow pattern. The flow pattern of sample 2 looks broken due to the improper heat generation, mainly due to low tool speed and intermediate pin depth (3mm) which restricted the uniform flow of material

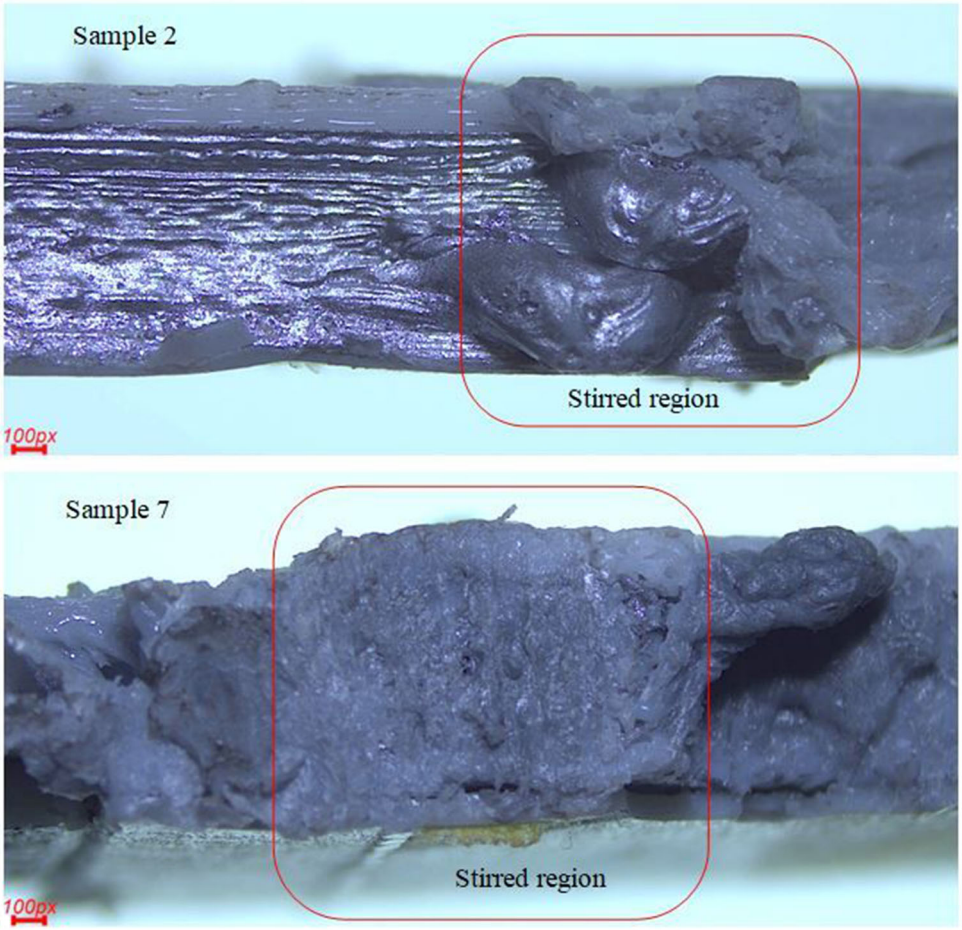


**Fig. 9** Cross-sectional view of welded (joints) sample 2 and sample 7

during FSW. On the other hand, low pin depth (2mm) may have been smoothening the flow (Also confirmed from the optical micrograph).

The formation of sound joint by FSW process of polymers or polymeric composites is highly dependent upon the selection of the process parameters. The right selection of levels of FSW process parameters more or less decides the quality of the weld, plus defects may be minimized if selection becomes optimum (Ref 37-42). In this study, the TRS (800rpm) with 3mm pin depth resulted in the flow of materials outside the stirred region which has been resulted in the excessive flow of the materials during FSW in case of sample 2 (see Fig. 9), whereas the control flow of materials has been observed with high TRS (1400rpm) and low depth of pin profile in case of sample 7. This may be due to the fact that low depth of pin profile has resulted in the controlled flow of materials during FSW toward reducing the defect formation caused by restricting excessive materials flow.

**4.2.2 Fracture Morphology by SEM Photomicrographs.** The SEM photomicrographs reveal the proper explanation of why UTS and FTS were observed maximum for sample 7 and minimum for sample 2. The photomicrographs of fractured joints of neat PLA have also been compared with these two for understanding the role of reinforcing Al and varying process parameters (refer to Fig. 10). In FSW, the joint strengths are mainly dependent upon a few factors such as control of materials flow during stirring, the impact of varying process parameters, control over adequate heat generation, and materials properties like thermal conductivity, crystallinity, glass transition temperature, melting temperature, etc. Low thermal conductivity and low crystallinity are major problems associated with the thermoplastic materials which minimized the joint strength if manufactured by the FSW (Ref 43, 44). The low thermal conductivity and crystallinity restrict the control of materials flow in FSW process. Low thermal conductivity and low crystallinity cause inadequate heat generation during FSW which minimized the mechanical strength. Also, inadequate heat generation and uncontrolled materials flow leads to the formation of large voids and cracks which lower the mechanical strength of the joints. To counter the above-mentioned issues which weaken the joint's strengths, two strategies have been made. Firstly, the Al layers have been deposited in between the PLA layer to enhance the thermal conductivity and secondly the FSW has been performed using a semi-consumable pin of similar materials which can compensate for the materials loss and void formation during FSW (Ref 28, 45).

In the case of fracture of neat PLA joints, a range of cracks has been observed with some surface asperities in the form of porous holes. This is caused by less heat formation during the stirring process due to the no reinforcement of Al metal. Similar observations have been observed for sample 2, in which non-mixed layers and surfaces have been observed. Also, the more magnified photomicrographs of sample 2 signified the forma-

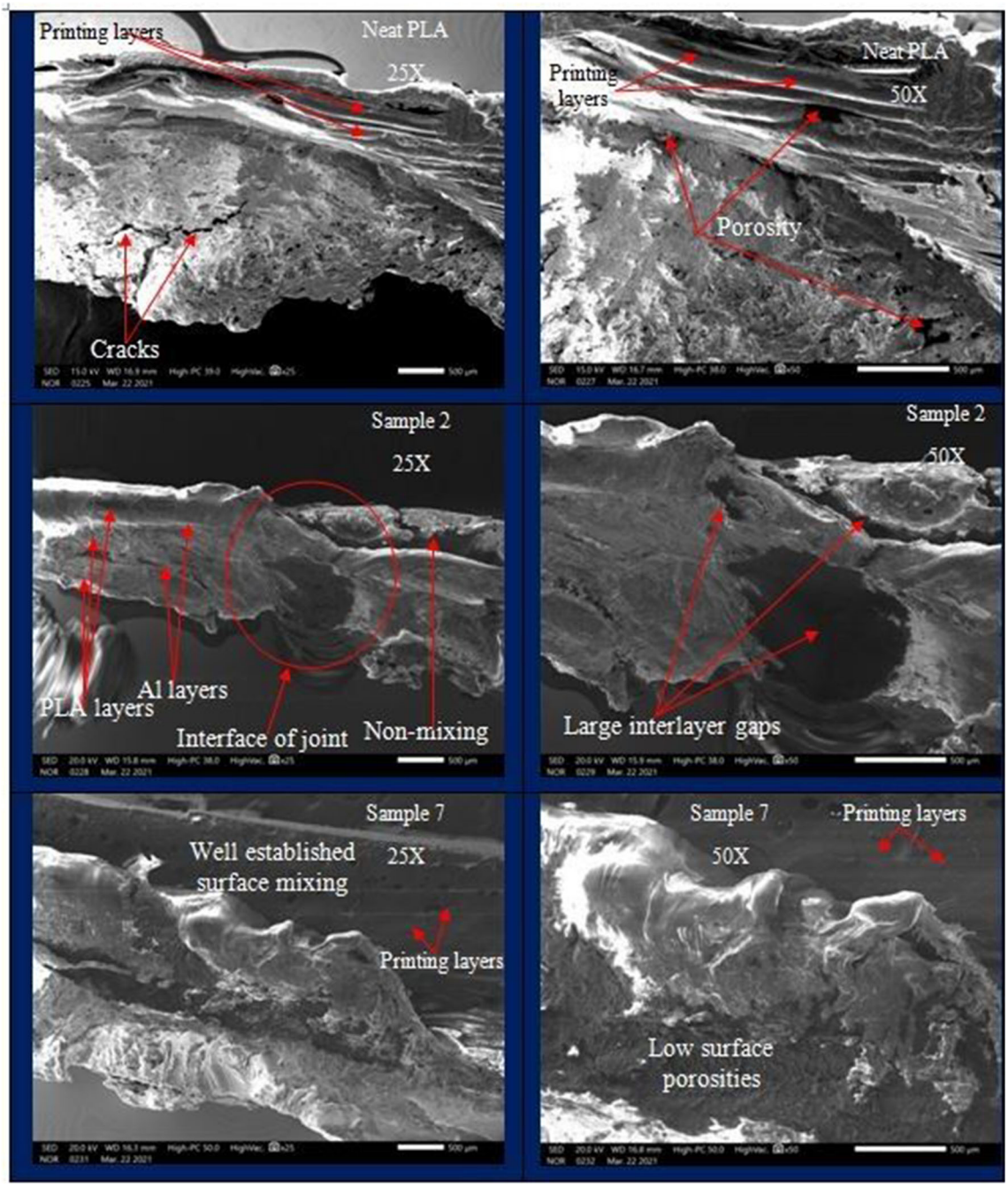


**Fig. 10** SEM photomicrographs of fractured surfaces of FSW-welded neat PLA, sample 2 and sample 7

tion of porous and blowholes which have been caused due to the low heat formation at the interface of the joints due to low TRS (800 rpm). On the other hand, the well-structured/patterned fracture has been observed in the joint of sample 7 which confirms the high UTS and FTS. Also, there are insignificant holes/pores/blowholes/cracks that have been observed in the case of the fractured joint of sample 7. Photomicrographs of fractured FSW-welded samples were processed through the Gwyddion 2.56 software package to investigate the fashion of fractures upon tensile loading (see Fig. 11). The rendered photomicrograph of fractures neat PLA joint has been observed with a sign of some stretched pores. There are two thick lines along the surface that signify the chances of non-mixing and crack formation due to less heat at the interface. But the involvement of high TRS of pin profile has been contributed likely for some extent of good mixing of PLA polymers. In the case of fractured fractures, the surface of sample 2, there is brittle fracture-like fashion has been observed with less significance of pore formation due to stretching by tensile loading.

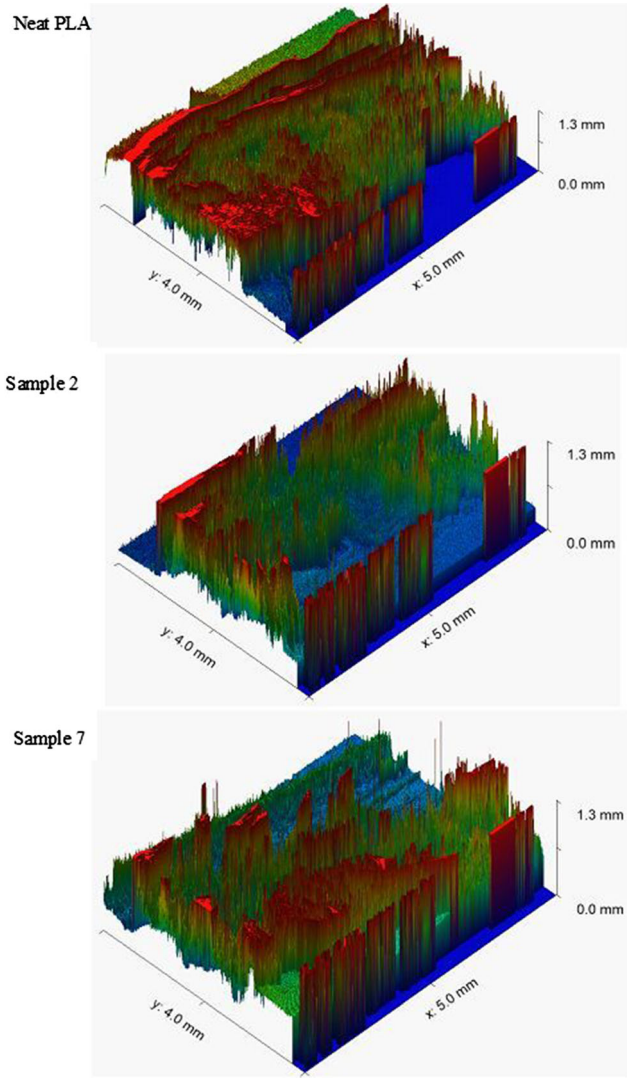


**Fig. 11** Rendering of fractured surfaces of welded joints

The high formation of defects in sample 2 is primarily due to the low TRS, which contributed to less heat generation for stirring/mixing of polymer. On the other hand, the fracture fashion of welded joint of sample 7 has been observed with pure brittle fracture. It has been observed several pores/stretched parts on the fractured joint, which contributed to better resistance against tensile loading in sample 7.

**4.2.3 EDS.** Figure 12 shows the EDS plots for fractured joints of neat PLA joint, sample 2 and sample 7. The EDS observations have been taken as confirmatory for variation over tensile properties. In the case of the fractured joint of near PLA, there is a high atomic carbon content (40.46 ± 0.77%) which must lead to hardening of surface to that fractured against less tensile loading; on the other hand, the presence of Al (3.89 ± 0.28%) in case of sample 7 has been led to increased heat formation which contributed toward better tensile properties. Comparing carbon content in sample 2 (38.10 ± 0.63%) and sample 7 (34.74 ± 0.28%), the higher carbon presence in sample 2 made the stirred surface hard and reduced the better stirring so that mechanical properties have resulted in minimum.

### 4.3 XRD

XRD measured the crystal structure of all three joints samples (neat PLA joint, sample 2, and sample 1) with Cu-Kα radiation (wavelength (λ) = 1.54060Å) at 40 kV and 25 mA. The diffraction patterns were collected at an angle, 2θ between 10 and 100.397° at a 5°/min scanning rate. It has been observed that joint of sample 7-based sample exhibits a maximum of 10 peaks (12.991°, 14.120°, 17.242°, 22.322°, 26.598°, 27.775°, 29.351°, 30.346°, 64.240°and 77.426°), whereas sample 2 exhibited five peaks (17.192°, 26.900°, 28.048°, 64.303°, and 77.500°) and neat PLA sample exhibited has only two peaks (28.079° and 77.340°). According to the standard database (PDF 00-064-1624) for PLA thermoplastic polymer with space group R-3(148) and a(Å): 10.653; b(Å): 6.131; c(Å): 28.810; a/b: 1.73756 and c/b: 4.69907 has been compared (Fig. 13).

Based on the database, it is noticed that all the peaks in each sample are matched with PLA thermoplastic polymer database with very marginal shifting that confirms the PLA polymer present in the samples. The crystal size, the ratio of crystalline to amorphous regions, the distance between the crystal planes, crystal arrangement pattern, and crystalline structure are all evaluated using XRD. This means that the XRD technique can monitor structural changes in crystalline materials caused by blending with other materials. As per previously reported work, PLA thermoplastic polymer has different crystallinity %age values as per thermal and other external factors (Ref 46). As per data given in Table 4, neat PLA has 25.30 % crystallinity, whereas sample 2 and sample 7 has 31.20% and 41.30 % crystallinity value. According to previously reported work, crystallinity directly affects the tensile strength (higher crystallinity has higher tensile strength) of that is a polymer. In the crystalline phase, the intermolecular bonding is more significant and supports the tensile testing results given in Table 2 (Ref 47). The higher crystallinity in the case of sample 7 has been assured the higher tensile strength, refer to Table 4.

### 4.4 FTIR

The FTIR spectrum based upon absorbance of IR rays by FSW PLA specimens is shown in Fig. 14. A significant variation in absorbance was obtained for incident IR waves with wave number (WN) ranging from 500 to 4000cm$^{-1}$. Absorbance spectrum of PLA (Fig. 12a) outlined that significant chemical structural changes were observed in FSW sample 2 (Fig. 12b) and sample 7 (Fig. 12c) at three distinct points, i.e., 3857cm$^{-1}$, 2340cm$^{-1}$ and 1125cm$^{-1}$ WN as compared to base polymer matrix. At 3857cm$^{-1}$ WN, a sharp peak shows the strong bonding of C=O in PLA. A slight shift in the peak at same WN range highlights the dislocation of C=O bond from its original position due to which weak mechanical strength was obtained in sample 2. The shifting of peak corresponds toward asymmetrical stretching of bonds that may result due to the formation of new bonds between the Al and C=O functional group present in PLA. The absorbance peaks at 2340cm$^{-1}$ WN in Fig. 12(a) corresponded toward the excitation of C-H functional group of FSW PLA, whereas Fig. 12(b) shows that the absorbance of IR rays decreased in same WN range for C-H group in case of sample 2. On the other hand, better processing conditions improved the absorbance peaks for C-H group of FSW composite as Fig. 12(c) shows that strong peaks were obtained for sample 7. Also, FSW PLA and its composite samples outlined the formation of a strong aldehyde

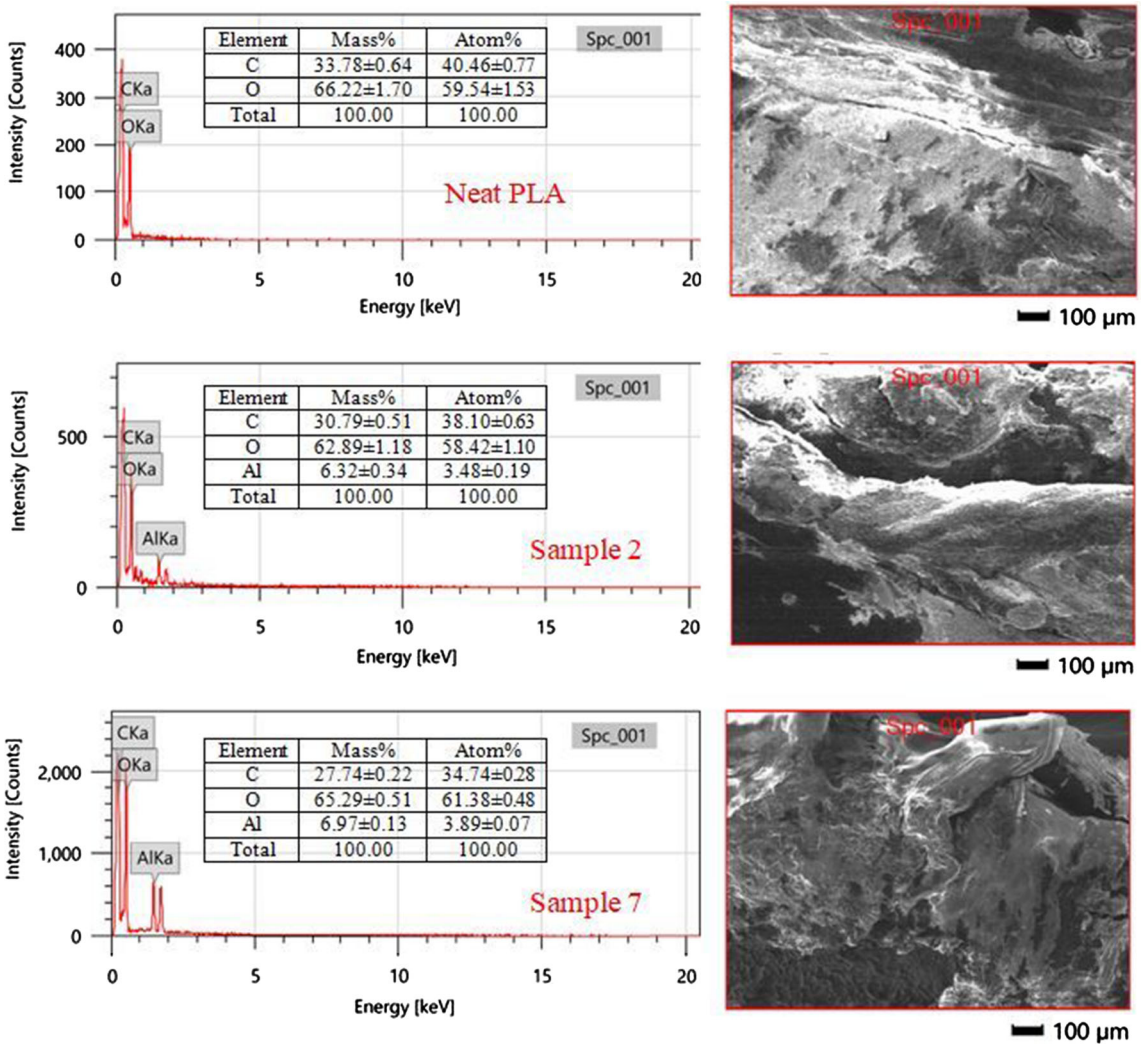


**Fig. 12** EDS on the fractured joint of neat PLA joint, sample 2 and sample 7

functional group at 1125 $cm^{-1}$ WN. With improved TRS and TVS conditions, the absorbance peaks at 1125 $cm^{-1}$ WN significantly increased for sample 7, whereas no large shift was observed in PLA and sample 2 for same 1125$cm^{-1}$ WN range. It may be stated that several Al spray coatings played a less significant role in improving the bonding properties of the FSW PLA matrix. On the other hand, fixing processing conditions, i.e., TRS, depth of pin, and TVS of FSW, may be more responsible for imparting better mechanical properties to the specimens. On behalf of FTIR analysis, adequate bonding strength in sample 7 was achieved due to higher TRS (1400 rpm) and intermediate TVS (40 mm/min).

### 4.5 Optimization of Tensile Properties

The hybrid multi-objective optimization for tensile properties (UTS, FTS, PEB, and MOT) has been executed in the process shown in Fig. 15.

**4.5.1 Regression Analysis.** Regression analysis is one of the most widely used techniques for interpreting variable data to deliver a good analysis and optimization strategy. The regression analysis is thus a combination of statistical methods, facilitating the estimation of relationships between a dependent variable and independent variables. In regression analysis, the outcome is predicted by the values of covariates or predictors. It can be used to determine the strength of the relationship between variables and find out the forthcoming relationship between them. Regression analysis may have variations, such as linear, multiple linear, and nonlinear. Linear and multiple linear are the most common methods. The mathematical model defines a relationship between independent and response parameters as shown in Eq 2:

$$Y = \beta_0 + \sum_i^n \beta_i \times C_i + \sum_i^n \beta_{ii} \times C^2{}_i + \sum_i^n \beta_{ij} \times C_i C_{ij} \quad \text{(Eq 2)}$$

Equation 2 can be written for six variables as shown in Eq 3, where $C_1$, $C_2$, $C_3$, $C_4$, $C_5$, $C_6$ are the process parameters, and Y denotes the response parameters.

$$Y = \beta_0 + \beta_1 \beta C_1 + \beta_2 C_2 + \beta_3 C_3 + \beta_4 C_4 + \beta_5 C_5 + \beta_6 C_6 + \beta_7 C_1 \times C_2 \quad \text{(Eq 3)}$$

In this research, there are three input variables, whereas UTS, FTS, PEB, and MOT are output parameters. Four single

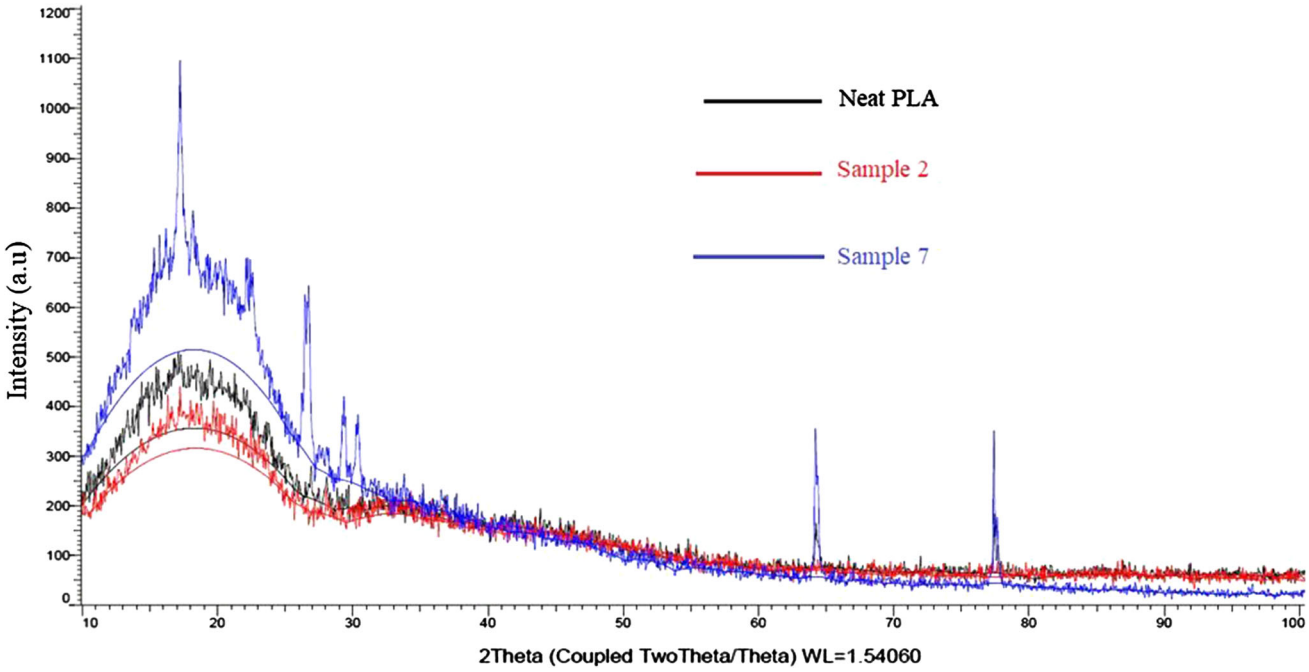


**Fig. 13** XRD spectra (Intensity vs. 2θ) of neat PLA, best and worst tensile strength with molecular weights is 234.2 with an orthorhombic crystal structure

**Table 4 XRD observations of neat PLA joint, sample 2, and sample**

| | Neat PLA | Sample 2 | Sample 7 |
|---|---|---|---|
| Crystallinity (in %age) | 25.300 | 31.200 | 41.300 |
| Amorphous (in %age) | 74.700 | 68.800 | 58.700 |
| Peak Angle (2θ) | | | 12.991° |
| | | | 14.120° |
| | | 17.192° | 17.242° |
| | 28.079° | 26.900° | 22.322° |
| | 77.340° | 28.048° | 26.598° |
| | | 64.303° | 27.775° |
| | | 77.500° | 29.351° |
| | | | 30.346° |
| | | | 64.240° |
| | | | 77.426° |

objective functions are developed, one for each output, using regression methods.

$$\begin{aligned}\mathrm{UTS_{MAX}} &= 114.9 + 0.02792A - 88.95B + 1.204C \\ &+ 0.000004A \times A + 15.38B \times B - 0.01900C \times C \\ &- 0.01037A \times B + 0.000003A \times C\end{aligned} \quad \text{(Eq 4)}$$

$$\begin{aligned}\mathrm{FTS_{MAX}} &= 103.4 + 0.02510A - 80.02B \\ &+ 1.083C + 0.000004A \times A + 13.84B \times B \\ &- 0.01712C \times C - 0.009333A \times B + 0.000004A \times C\end{aligned} \quad \text{(Eq 5)}$$

$$\begin{aligned}\mathrm{PEB_{MAX}} &= 29.04 + 0.000185A - 13.83B \\ &- 0.3556C - 0.000002A \times A + 2.167B \times B \\ &+ 0.003333C \times C - 0.000000A \times B + 0.000111A \times C\end{aligned} \quad \text{(Eq 6)}$$

$$\begin{aligned}\mathrm{MOT_{MAX}} &= 3.389 + 0.000956A - 2.472B \\ &+ 0.01378C - 0.000000A \times A + 0.3833B \times B \\ &- 0.000213C \times C - 0.000066A \times B - 0.000002A \times C\end{aligned} \quad \text{(Eq 7)}$$

**4.5.2 AHP.** AHP is a mathematical tool of problem-solving, organizing, and analyzing complex decisions, using math and psychology It was developed by Thomas L. Saaty in the 1970s and has been refined by many researchers since then and became popular in the late 1990s and early 2000s. AHP provides a logical framework for a requisite result by quantifying its criteria and alternative options and associating those elements with the overall goal. Table 5 shows the amount of subjective weight for each property.

Objective weights of attributes can be determined using the statistical variance concept. The steps involved in finding the values of objective weights are mentioned below:

i. Step 1 Decision matrix: The values of attributes in a tabular form
ii. Step 2 Normalized matrix: The normalized matrix can be developed using Eq (8)

$$rij = aij / \sum_{i}^{n} aij \quad \text{(Eq 8)}$$

where $a_{ij}$ = decision matrix; n = number of entries in the column

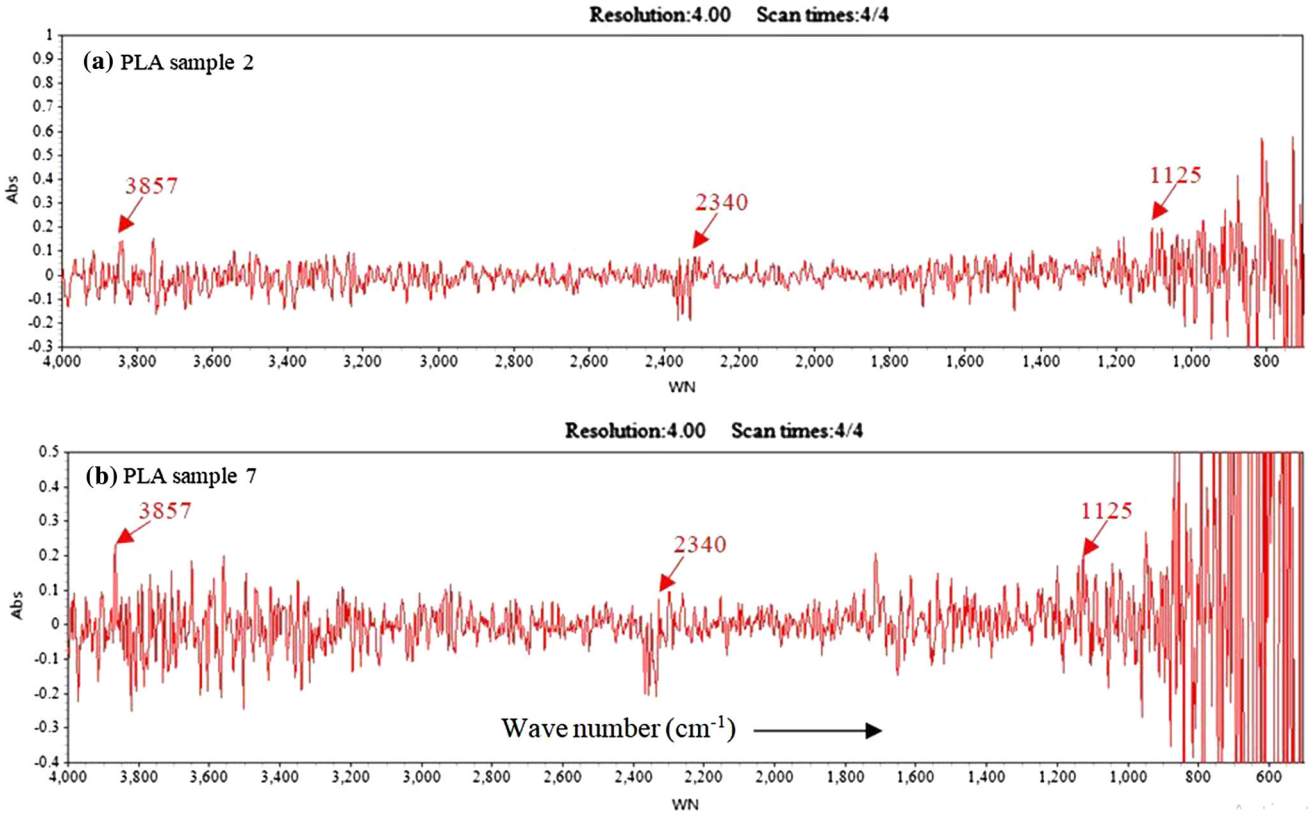


**Fig. 14** FTIR-based absorption spectrum of joints sample of neat PLA (a), sample 2 (b) and sample 7(c)

**Table 5 Subjective weights for tensile properties**

| | UTS | FTS | PEB | MOT | Subjective Weights |
|---|---|---|---|---|---|
| UTS | 1.00 | 1.00 | 3.00 | 0.50 | 0.23 |
| FTS | 1.00 | 1.00 | 3.00 | 0.50 | 0.23 |
| PEB | 0.33 | 0.33 | 1.00 | 0.25 | 0.16 |
| MOT | 2.00 | 2.00 | 4.00 | 1.00 | 0.38 |

**Table 6 Objective weights for tensile properties**

| | UTS | FTS | PEB | MOT |
|---|---|---|---|---|
| Equal Weights | 0.25 | 0.25 | 0.25 | 0.25 |
| Subjective Weights | 0.24 | 0.24 | 0.09 | 0.43 |
| Objective Weights | 0.19 | 0.19 | 0.16 | 0.46 |
| Hybrid Weights | 0.23 | 0.23 | 0.16 | 0.38 |

iii. Step 3 Compute the values of statistical Variance: The values of statistical variance ($Vi$) are found using Eq (9):

$$Vi = \frac{1}{n}\sum_{i=1}^{n}\{rij - (rij)\text{mean}\}^2 \quad \text{(Eq 9)}$$

iv. Step 4 Determine objective weights: The objective weights ($W_i$) are computed using Eq (10);

$$Wi = \frac{Vi}{\sum_{i=1}^{n} Vi} \quad \text{(Eq 10)}$$

The hybrid weights are computed using the geometric mean of AHP and Equal weights. Each value of the geometric mean is divided by the sum of all geometric values. The objective weights assigned to different response parameters are shown in Table 6.

$Z_{MIN}$ is the goal to attain the maximum values of all response parameters. It can be defined by given Eq (11).

$$\begin{aligned} Z_{\text{MIN}} = &-W_1(114.9 + 0.02792A - 88.95B + 1.204C \\ &+ 0.000004A \times A + 15.38B \times B - 0.01900C \times C - 0.01037A \times B \\ &+ 0.000003A \times C) - -W_2(103.4 + 0.02510A - 80.02B \\ &+ 1.083C + 0.000004A \times A + 13.84B \times B - 0.01712C \times C \\ &- 0.009333A \times B + 0.000004A \times C) - W_3 29.04 + 0.000185A \\ &- 13.83B - 0.3556C - 0.000002A \times A + 2.167B \times B + 0.003333C \times C \\ &- 0.000000A \times B + 0.000111A \times C - W_4(3.389 + 0.000956A \\ &- 2.472B + 0.01378C - 0.000000A \times A + 0.3833B \times B - 0.000213C \times C \\ &- 0.000066A \times B - 0.000002A \times C) \end{aligned} \quad \text{(Eq 11)}$$

**4.5.3 GA.** GAs is search and optimization techniques based on genetics and natural selection. It has been successfully applied to a broad range of real-world problems of high complexity. A GA can be used for solving both constrained and unconstrained optimization problems. The algorithm generates a group of points at every iteration. The best point in the group formulates an optimal solution. GA provides a list of reasonable solutions rather than one single solution in a faster and more

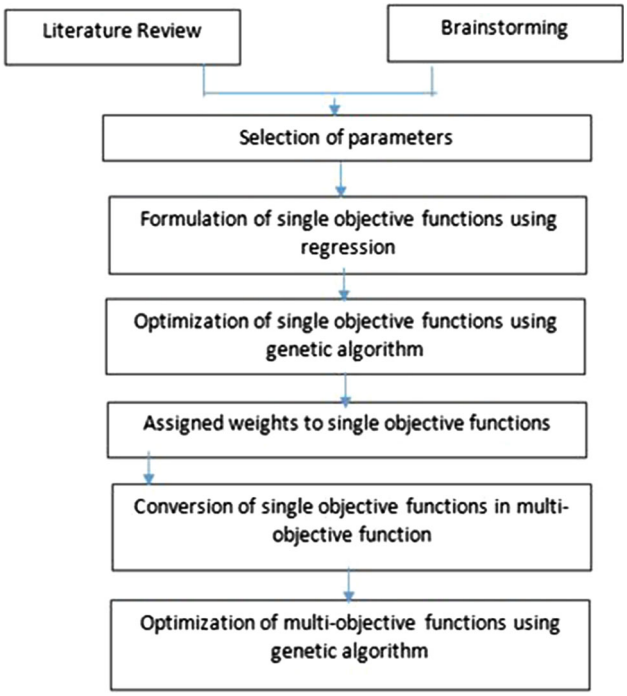


**Fig. 15** Hybrid multi-objective approach for optimization of tensile properties

efficient manner when compared to the other traditional methods. It is useful when the search area is very large and has a large number of involved parameters. The steps required for the implementation of GA are shown in Fig. 16.

Table 7 displays the single and multi-objective goals for response parameters. In the case of a single objective, it is required to maximize all four tensile properties. On the other hand, the purposes of multi-objective optimization are to minimize as equal weights are assigned to all the response parameters. It can be noticed that the values of TRS, SPD, and TVS are the same during UTS maximization and multi-objective using AHP weights. Generally, the optimum value of TRS remains the same for all the conditions except the single objective optimization of FTS and PEB. Also, the value of SPD is the same for all the conditions, whereas TVS is also approximately the same except for a single objective PEB. The optimized levels of input parameters can be used to attain desired results as per goal, such as single objective or multi-objective.

The number of iterations performed by GA is vital to notice as this defines the complexity of the optimization problem. The lesser number of iterations indicates a simple and easy solution, whereas higher values of generations imply the complex nature of the problem. Figure 17 shows the best, mean and worst values attained at different iterations during multi-objective optimization. It can be noticed that best fitness and mean fitness values are achieved at generations lesser than 100. Also, the best, worst, and mean scores are attained in less than 100 generations which implies the average complexity experienced while finding appropriate solutions to the optimization problem.

Figure 18 plots the response surface plots depicting the impact of TRS and TVS on FTS. It can be observed that both extreme levels of TRS lead to an increase in FTS, whereas the

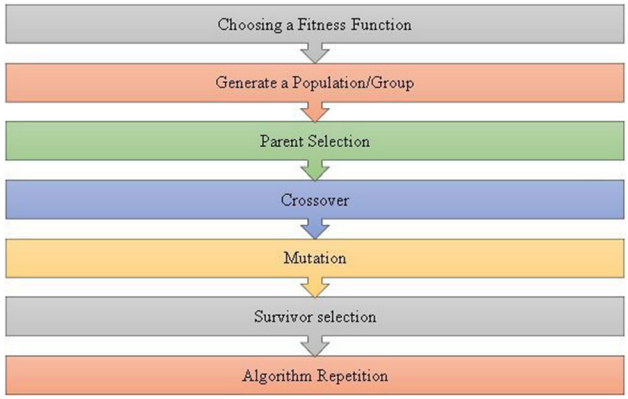


**Fig. 16** Steps required for the implementation of GA

**Table 7 Single and multi-objective optimization results**

| Optimization | Notation | TRS | SPD | TVS |
|---|---|---|---|---|
| Single objective | $UTS_{MAX}$ | 1400.00 | 2.00 | 31.79 |
| Single objective | $FTS_{MAX}$ | 1358.15 | 2.00 | 31.30 |
| Single objective | $PEB_{MAX}$ | 800.00 | 2.00 | 20.00 |
| Multi-objective using Equal weights | $MOT_{MAX}$ | 1400.00 | 2.00 | 31.93 |
| Multi-objective using AHP weights | $Z_{MIN}$ | 1400.00 | 2.00 | 31.79 |
| Multi-objective using Objective weights | $Z_{MIN}$ | 1400.00 | 2.00 | 31.85 |
| Multi-objective using Hybrid weights | $Z_{MIN}$ | 1400.00 | 2.00 | 31.85 |

medium level of TRS results in decreased value of FTS. On the other hand, with an increase in levels of TVS, the FTS continues to increase up to 1400 rpm. The combined levels of both TVS and TRS are excellent conditions for the maximization of FTS.

In Fig. 19, the impact of TRS and TVS on the response (PEB) has been plotted using response surfaces. The yellow-colored surface depicts optimum levels of input parameters like the maximum value of PEB was attained. Hence, it is recommended to use lower levels of TVS and higher levels of TRS for acquiring the best response in terms of PEB. However, from 25-35 mm/min. TVS, the minimum value of PEB, was attained as per response surface plots. Also, the response again increases slightly as there is a further increase in levels of TVS. The suggested levels of TRS and TVS are 20 mm/min. and 800 rpm, respectively, for maximization of PEB.

Figure 20 shows the response surface plots depicting the impact of SPD and TVS on MOT. It has been observed that the effect of lower levels of SPD supports the increment in the value of MOT. On the other hand, the higher levels of TVS are most favorable for the maximization of MOT. Thus, to attain the maximized value of MOT, the SPD and TVS must be maintained at 2mm SPD and 40 mm/min TVS, respectively. Figure 21 shows the impact of TRS and SPD on UTS, which is one of the most critical parameters considered during the tensile testing of materials. It can be noticed that the medium levels of SPD do not support the enhancement of UTS.

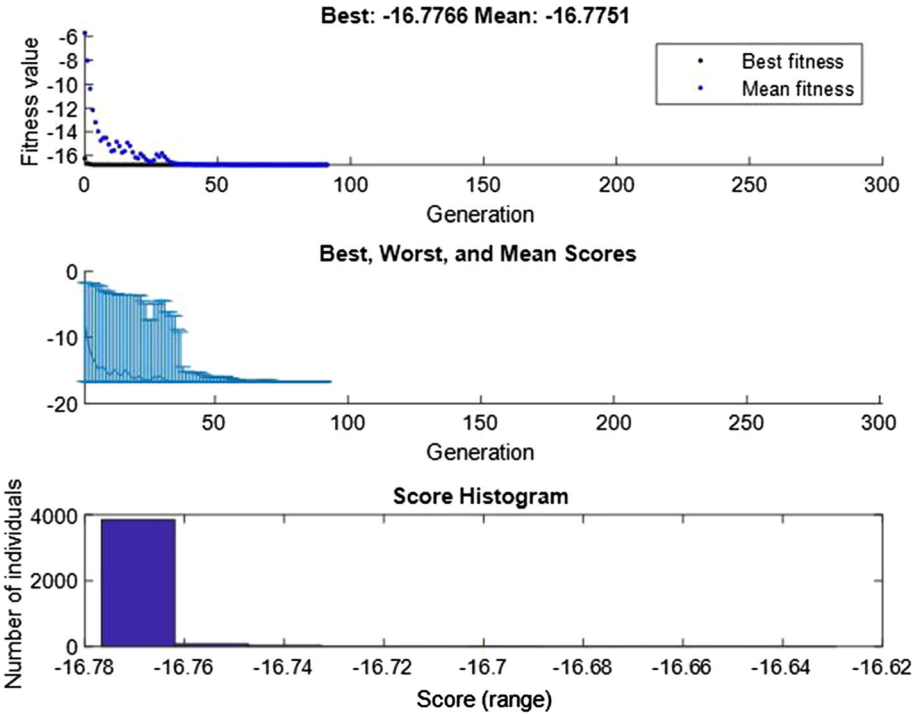


**Fig. 17** Best values attained at different iterations

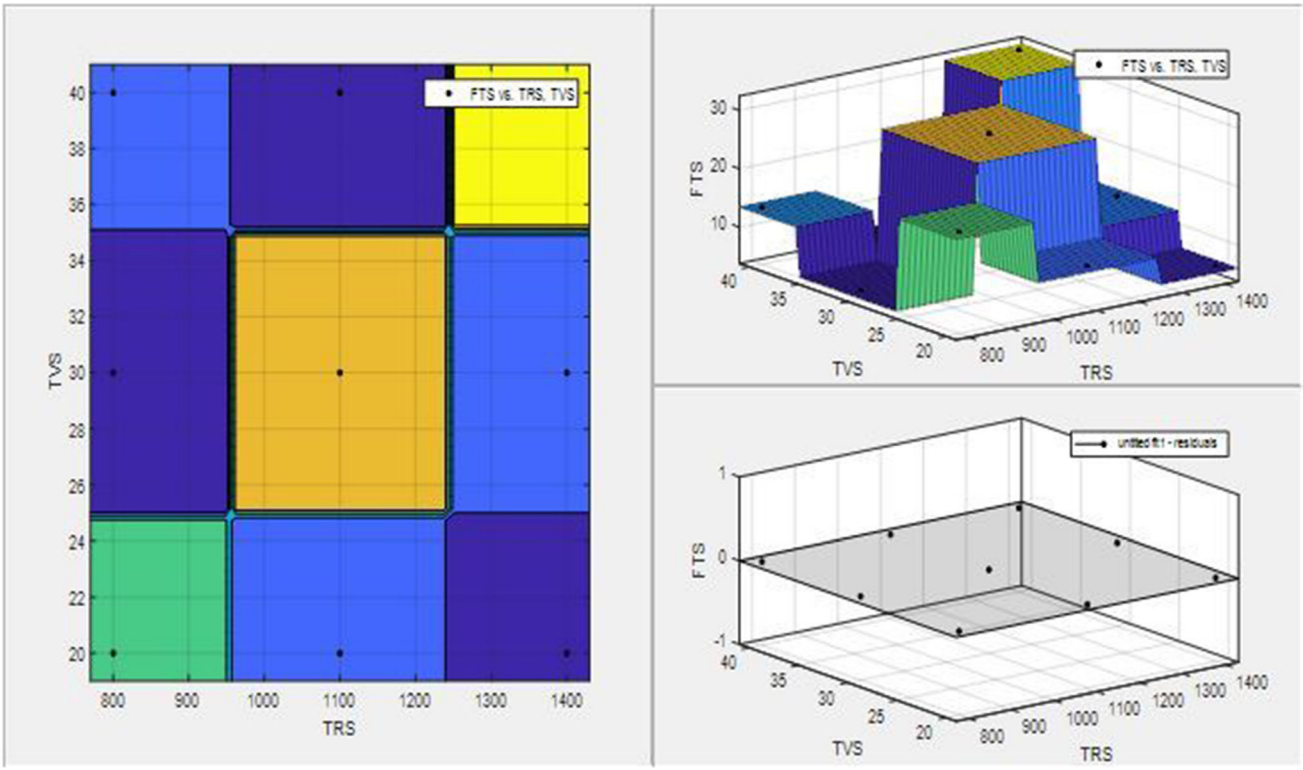


**Fig. 18** Effect of TRS and TVS on FTS

Also, the lesser values of UTS have been attained at lower TRS. Hence, it is recommended that the optimum levels of TRS and SPD must be 1400 rpm and 2 mm, respectively. To summarize, the individual impact of each input parameter is different. Hence, to attain maximum values of all the four tensile properties, the levels suggested by AHP must be maintained during the manufacturing process.

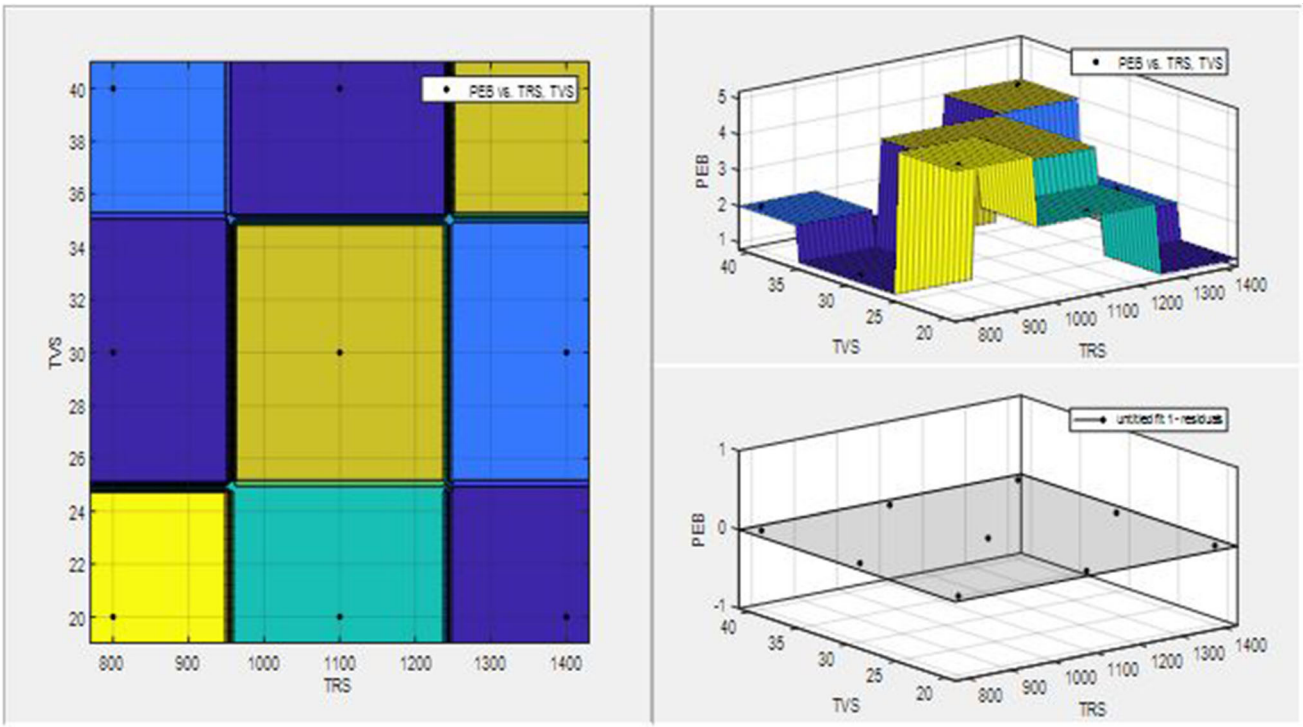


**Fig. 19** Effect of TRS and TVS on PEB

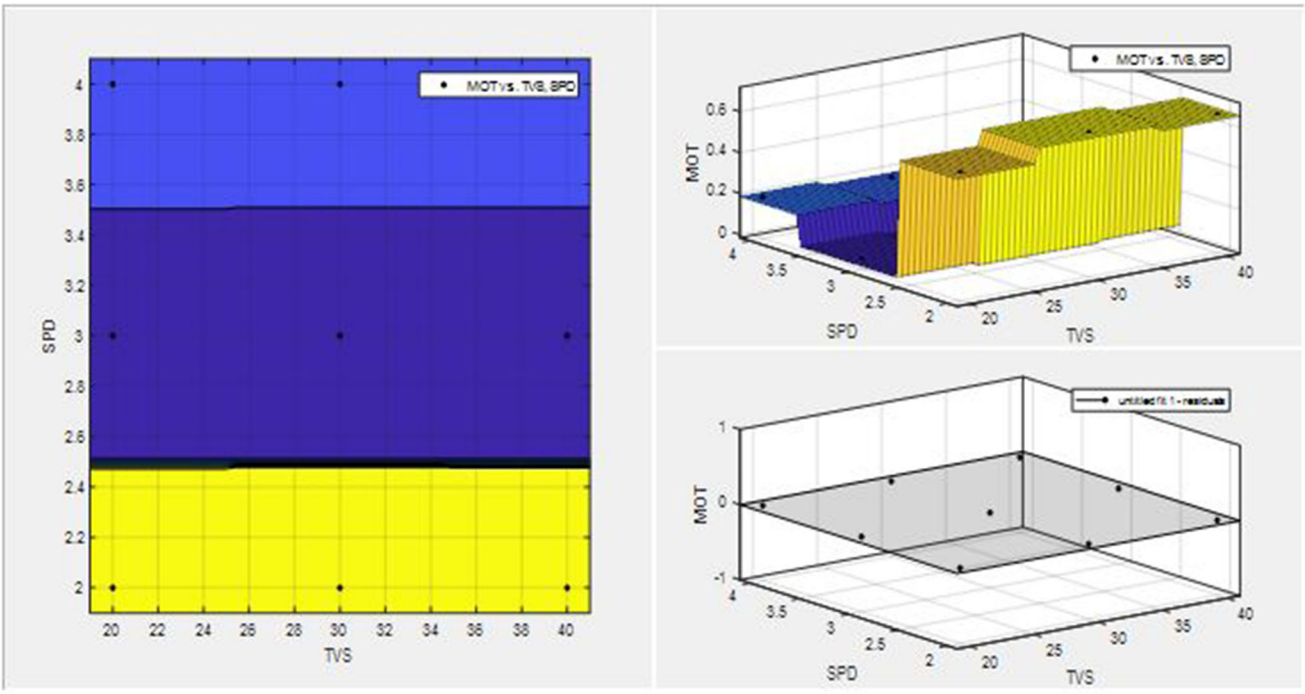


**Fig. 20** Effect of SPD and TVS on MOT

## 5. Conclusions

Following are the conclusions of the present study.

i. The tensile strength in the case of sample 7 was exhibited due to the combination of higher TRS (1400 rpm) and TVS (40 mm/min), which provided better heat generation at the joint interface to promote the stirring/fusion. On the other hand, insufficient heat formation due to lower TRS (800rpm) and TVS (30 mm/min) were unable to produce adequate heat for stirring, so that it has been observed as minimum tensile strength for sample 2.

ii. A significant non-mixing/non-stirring region has been observed in sample 2 due to low TRS, as well as well-

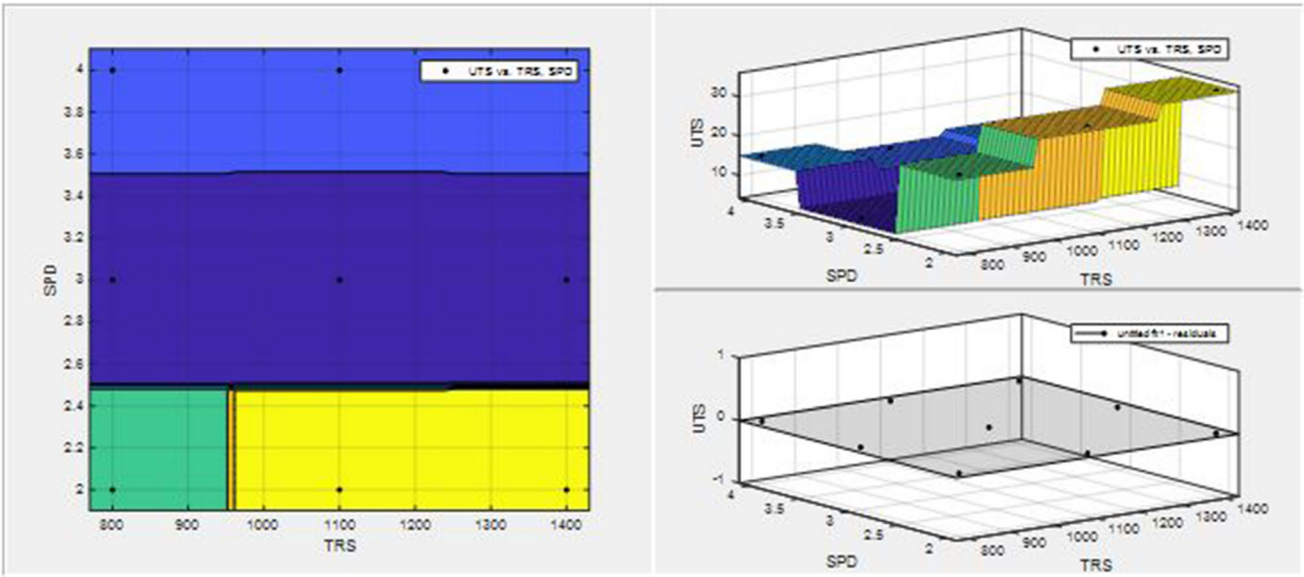


**Fig. 21** Effect of TRS and SPD on UTS

structured/well-stirred surface was observed for sample 7 due to high TRS as confirmed by SEM and optical microscopes.

iii. The deposition of Al microlayers in between PLA layers has increased crystallinity (As confirmed by XRD analysis), responsible for higher mechanical properties in the final weld. It is confirmed by FTIR analysis that a better FSW setting in welding of sample 7 has led to better binding, which provided better tensile properties.

iv. Response surface plots showed the conflicting levels for each response which could not be used for attaining the maximized level of each response. AHP and GA are implemented to acquire a single set of parameters that would result in the best value of each response, i.e., UTS, FTS, PEB, and MOT. The suggested levels are 1400 rpm, 2 mm, and 31.79 mm/min. of TRS, SPD, and TVS, respectively, as per AHP.

## Acknowledgment

The authors are highly thankful to University Centre for Research and Development, Chandigarh University and Centre for Manufacturing Research, Guru Nanak Dev Engineering College, Ludhiana, for technical and testing support in this manuscript.

## References

1. F. Lambiase, D. Hamed Aghajani and S. Abdolreza, Friction Stir Welding and Friction Spot Stir Welding Processes of Polymers—State of the Art, *Materials*, 2020, **13**(10), p 2291
2. D. Hamed Aghajani and A. Simchi, Experimental and Thermomechanical Analysis of the Effect of Tool Pin Profile on the Friction Stir Welding of Poly (Methyl Methacrylate) Sheets, *J. Manuf. Process*, 2018, **34**, p 412–423
3. D.H. Aghajani, F. Khodabakhshi and A. Simchi, Evaluation of a Polymer-Steel Laminated Sheet Composite Structure Produced by Friction Stir Additive Manufacturing (FSAM) Technology, *Polym. Test.*, 2020, **90**, p 106690
4. D.H. Aghajani and A. Simchi, Experimental and Thermomechanical Analysis of Friction Stir Welding of Poly (Methyl Methacrylate) Sheets, *Sci. Technol. Weld. Join.*, 2018, **23**(3), p 209–218
5. E. Majid and D.H. Aghajani, Experimental and Thermomechanical Study on FSW of PMMA Polymer T-Joint, *Int. J. Adv. Manuf. Technol.*, 2018, **97**(1–4), p 1445–1456
6. D.H. Aghajani, A. Simchi and F. Lambiase, Friction Stir Welding of Polycarbonate Lap Joints: Relationship Between Processing Parameters and Mechanical Properties, *Polym. Test.*, 2019, **79**, p 105999
7. D.H. Aghajani, A. Eyvazian and A. Simchi, Modeling and Experimental Validation of Material Flow During FSW of Polycarbonate, *Mater. Today Commun.*, 2020, **22**, p 100796
8. E. Arameh, A.M. Hamouda, D.H. Aghajani and M. Elyasi, Study on the Effects of Tool Tile Angle, Offset and Plunge Depth on Friction Stir Welding of Poly (Methyl Methacrylate) T-Joint, *Proc. Instit. Mech. Eng., Part B: J. Eng. Manuf.*, 2020, **234**(4), p 773–787
9. D.H. Aghajani, E. Garcia and M. Elyasi, Underwater Friction Stir Welding of PC: Experimental Study and Thermo-Mechanical Modelling, *J Manuf. Process.*, 2021, **65**, p 161–173
10. D.H. Aghajani and A. Simchi, Processing and Characterizations of Polycarbonate/Alumina Nanocomposites by Additive Powder Fed Friction Stir Processing, *Thin-Walled Structures*, 2020, **157**, p 107086
11. D.H. Aghajani and A. Simchi, Effects of Alumina Nanoparticles on the Microstructure, Strength and Wear Resistance of Poly (Methyl Methacrylate)-Based Nanocomposites Prepared by Friction Stir Processing, *J. Mech. Behav. Biomed. Mater.*, 2018, **79**, p 246–253
12. S.H. Masood and W.Q. Song, Development of New Metal/Polymer Materials for Rapid Tooling using Fused Deposition modelling, *Mater. Des.*, 2004, **25**(7), p 587–594
13. S.S. Sharifabad, H.A. Derazkola, M. Esfandyar, M. Elyasi and F. Khodabakhshi, Mechanical Properties of HA@ Ag/PLA Nanocomposite Structures Prepared by Extrusion-Based Additive Manufacturing, *J. Mech. Behav. Biomed. Mater.*, 2021, **1**(118), p 104455
14. R. Kumar, R. Singh, I.P.S. Ahuja and M.S.J. Hashmi, Friction-Stir-Spot Welding of 3D printed ABS and PA6 Composites: Flexural, Thermal and Morphological Investigations, *Adv. Mater. Process. Technol.*, 2020, **35**, p 1–8
15. J. Singh, R. Singh, R. Kumar, M.M. Rahman and S. Ramakrishna, PLA-PEKK-HAp-CS Composite Scaffold Joining With Friction Stir Spot Welding, *J. Thermoplastic Compos. Mater.*, 2019, **34**, p 74–764
16. R.K. Nath, P. Maji and J.D. Barma, Joining of Advance Engineering Thermoplastic Using Novel Self-Heated FSW Tool, *JOM.*, 2021, **28**, p 1–2
17. S. Singh, C. Prakash and M.K. Gupta, *On Friction-Stir Welding of 3D Printed Thermoplastics. InMaterials Forming, Machining and Post Processing*, Springer, Cham, 2020

18. R. Singh, R. Kumar and I.P. Ahuja, Friction Welding for Functional Prototypes of PA6 and ABS with Al Powder Reinforcement, *Proc. Natl. Acad. Sci., India, Sect. A*, 2020, **7**, p 1–9
19. R. Kumar, R. Singh, I.P. Ahuja and A. Fortunato, Thermo-MECHANICAL Investigations for the Joining of Thermoplastic Composite Structures via Friction Stir Spot Welding, *Compos. Struct.*, 2020, **253**, p 112772
20. R. Kumar, R. Singh, I.P. Ahuja and M.S. Hashmi, Friction-Stir-Spot Welding of 3D Printed ABS and PA6 Composites: Flexural, Thermal and Morphological Investigations, *Adv. Mater. Process. Technol.*, 2020, **21**, p 1–8
21. F. Lambiase, V. Grossi and A. Paoletti, Effect of Tilt Angle in FSW of Polycarbonate Sheets in Butt Configuration, *Int. J. Adv. Manuf. Technol.*, 2020, **107**(1), p 489–501
22. A.K. Sharma, M.R. Choudhury and K. Debnath, Experimental Investigation of Friction Stir Welding of PLA, *Weld. World.*, 2020, **19**, p 1–1
23. H. Koçak, Surface Modification of a Model Part Produced with 3D Printing from PLA Material by Means of Composite Coating, *J. Mater. Eng. Perform.*, 2021, **31**, p 1–8
24. C. Prakash, G. Singh, S. Singh, W.L. Linda, H.Y. Zheng, S. Ramakrishna and R. Narayan, Mechanical Reliability and In Vitro Bioactivity of 3D-Printed Porous Polylactic Acid-Hydroxyapatite Scaffold, *J. Mater. Eng. Perform.*, 2021, **4**, p 1–1
25. U.K. Komal, B.K. Kasaudhan and I. Singh, Comparative Performance Analysis of Polylactic Acid Parts Fabricated by 3D Printing and Injection Molding, *J. Mater. Eng. Perform.*, 2021, **20**, p 1–7
26. P. Kumar, D.K. Rajak, M. Abubakar, S.G. Ali and M. Hussain, 3D Printing Technology for Biomedical Practice: A Review, *J. Mater. Eng. Perform.*, 2021, **26**, p 1–4
27. R. Kumar, J.S. Chohan, R. Kumar, A. Yadav and N. Singh, Hybrid FUSED Filament Fabrication for Manufacturing of Al Microfilm REINFORCED PLA Structures, *J. Braz. Soc. Mech. Sci. Eng.*, 2020, **42**(9), p 1–13
28. Kumar R, Chohan JS, Kumar R, Yadav A, Piyush, Kumar P. Metal spray layered hybrid additive manufacturing of PLA composite structures: Mechanical, thermal and morphological properties. Journal of Thermoplastic Composite Materials. 2020 Jun 24:0892705720932622
29. Wurth India Ltd. Perfect aluminium spray. https://eshop.wuerth.in/Perfect-aluminium-spraymatt-ALUSPR-PLUS-400ML/0893114115.sku/en/US/INR/ (accessed 27 April 2020)
30. M. Hassan, L. Chong and N. Sultana, Wettability and Water Uptake Properties of pla and pcl/gelatin-Based Electrospun Scaffolds, *ARPN J. Eng. Appl. Sci.*, 2006, **11**, p 13604–13607
31. M.F. Afrose, S.H. Masood, M. Nikzad and P. Iovenitti, Effects of Build Orientations on Tensile Properties of PLA Material Processed by FDM, *Adv. Mater. Res.*, 2014, **1044**, p 31–34
32. L. Deng, C. Xu, X. Wang and Z. Wang, Supertoughened Polylactide Binary Blend with High Heat Deflection Temperature Achieved by Thermal Annealing Above the Glass Transition Temperature, *Acs Sustain. Chem. Eng.*, 2018, **6**(1), p 480–490
33. S. Iannace, L. Sorrentino and E. Di Maio, *Biodegradable Biomedical Foam Scaffolds. InBiomedical Foams for Tissue Engineering Applications*, Woodhead Publishing, 2014
34. X. Tian, T. Liu, C. Yang, Q. Wang and D. Li, Interface and Performance of 3D Printed Continuous Carbon Fiber Reinforced PLA Composites, *Compos. A Appl. Sci. Manuf.*, 2016, **1**(88), p 198–205
35. O. Vambol, A. Kondratiev, S. Purhina and M. Shevtsova, Determining the Parameters for a 3D-Printing Process Using the Fused Deposition Modeling in Order To Manufacture an Article With the Required Structural Parameters, *Eastern-Eur. J. Enterprise Technol.*, 2021, **2**(1), p 110
36. A. Haleem, V. Kumar and L. Kumar, Mathematical Modelling & Pressure Drop Analysis of Fused Deposition Modelling Feed Wire, *Int. J. Eng. Technol.*, 2017, **9**(4), p 2885–2894
37. H.A. Derazkola and F. Khodabakhshi, Development of FED Friction-Stir (FFS) Process for Dissimilar Nanocomposite Welding between AA2024 Aluminum Alloy and Polycarbonate (PC), *J. Manuf. Process.*, 2020, **1**(54), p 262–273
38. H.A. Derazkola and F. Khodabakhshi, A Novel Fed Friction-STIR (FFS) Technology for Nanocomposite Joining, *Sci. Technol. Weld. Join.*, 2020, **25**(2), p 89–100
39. H.A. Derazkola and A. Simchi, A New Procedure for the Fabrication of Dissimilar Joints Through Injection of Colloidal nanoparticles During Friction Stir Processing: Proof Concept for AA6062/PMMA Joints, *J. Manuf. Process.*, 2020, **1**(49), p 335–343
40. H.A. Derazkola and M. Elyasi, The Influence of Process Parameters in Friction Stir Welding of Al-Mg alloy and Polycarbonate, *J. Manuf. Process.*, 2018, **1**(35), p 88–98
41. H.A. Derazkola, R.K. Fard and F. Khodabakhshi, Effects of Processing Parameters on the Characteristics of Dissimilar Friction-Stir-Welded Joints Between AA5058 Aluminum Alloy and PMMA Polymer, *Weld. World.*, 2018, **62**(1), p 117–130
42. H.A. Derazkola and A. Simchi, An Investigation on the Dissimilar Friction Stir Welding of T-Joints Between AA5754 Aluminum Alloy and Poly (Methyl Methacrylate), *Thin-Walled Struct.*, 2019, **1**(135), p 376–384
43. S.K. Sahu, D. Mishra, R.P. Mahto, V.M. Sharma, S.K. Pal, K. Pal, S. Banerjee and P. Dash, Friction Stir Welding of Polypropylene Sheet, *Eng. Sci. Technol. Int J.*, 2018, **21**(2), p 245–254
44. Y. Huang, X. Meng, Y. Xie, L. Wan, Z. Lv, J. Cao and J. Feng, Friction Stir Welding/Processing of Polymers and Polymer Matrix Composites, *Compos. A Appl. Sci. Manuf.*, 2018, **1**(105), p 235–257
45. J. Singh, R. Singh, R. Kumar, M.M. Rahman and S. Ramakrishna, PLA-PEKK-HAp-CS Composite Scaffold JOINING with Friction Stir spot Welding, *J. Thermoplast. Compos. Mater.*, 2021, **34**(6), p 745–764
46. S. Farah, D.G. Anderson and R. Langer, Physical and Mechanical Properties of PLA, and their Functions in Widespread Applications—A COMPREHENSIVE Review, *Adv. Drug Deliv. Rev.*, 2016, **15**(107), p 367–392
47. K. Balani, V. Verma, A. Agarwal and R. Narayan, Physical, Thermal, and Mechanical Properties of Polymers, *Biosurf A Mater Sci Eng Perspect*, 2015, **44**, p 329